TECHNISCHE UNIVERSITÄT WIEN
Vienna University of Technology

Diplomarbeit

Variation der Substrattemperatur während der Abscheidung von Kupfer, Indium, Gallium und Selen für Dünnschichtsolarzellen

Ausgeführt am

Atominstitut

in Zusammenarbeit mit dem

Ångström Solar Center
Uppsala Universitet, Schweden

unter der Anleitung von

Ao.Univ.Prof.DI Dr. Johann Summhammer

und

Dr. Marika Edoff

Dr. Uwe Zimmerman

(Uppsala Universitet)

durch

Lukas Plessing

9406670

Wien, 16 Dezember 2013   Lukas Plessing

2

Acknowledgement

Without the great support which I received from many sides I would not have been able to present this work. Therefore I would like to acknowledge:

Johann Summhammer for encouraging and supporting me on my way into photovoltaic research. It was him who supervised my research activities in Switzerland and in Sweden.

Uwe Zimmermann whose support for me went far beyond that of a supervisor. He was my guide in the laboratory and taught me not only to use and understand all kinds of tools and machinery, but also to repair and build them. I would like to thank him not only for the precious time he spent for me in the lab but also for taking the time for intense and detailed conversations about the matter.

Marika Edoff for strongly supporting me to come to Sweden with my family for the diploma thesis. She was a great supervisor and guided my work helping me in many discussions with her outstanding experience in CIGS based photovoltaics.

The whole team at the Angstrom solar center for the generous support and fruitful discussions. And for making Sweden not only place of great science but also a warm home for me and my family.

Ayodhya Tiwari for the invitation to the fabulous research group at the EMPA. Here I had the great opportunity to enter the world of thin film solar cells.

Special thanks to my family and friends for their continuous and stalwart backing.

Sammanfattning

I det här arbetet har påverkan av olika substrattemperaturprofiler under beläggningen av CIGS undersökts. CIGS samförångades på Mo-belagt substratglas i ett Inline-system. Kompletta solceller tillverkades av proverna som därefter undersöktes. I tre serier av experiment förångades CIGS med fyra olika substrat temperatur profiler. Under den första experimentserien hölls temperturen konstant, och beläggningarna tillverkades med fyra olika substrattemperaturer. I början av förångahingen vid de följande två experimenten sönktes temperaturen stegvis. Mot slutet av förångahingen nådde temperaturen den ursprungligen nivån. Från alla prover tillverkades Glas/Mo/CIGS/CdS/ZnO solceller. Tjockleken och sammansättningen av CIGS-lagren mättes och utvärderades. Från solcellerna gjordes mätningar av strömspänningskurvor och kvanteffektivitet. Som komplettering togs även bilder av en del av proverna i elektronmikroskop.

Abstract

In this work the influence of different substrate temperature profiles during CIGS deposition was examined. CIGS was co-evaporated on Mo coated glass substrates. Subsequently the samples were processed to complete solar cells. The solar cells and the CIGS layer were analysed.

In three series of experiments CIGS was deposited. In each series four variations of the temperature profile have been applied. In the first series of experiments the temperature was kept constant. Four depositions at different temperatures were accomplished. In the two following series of experiments the starting temperature of the deposition was reduced stepwise. In the final series at the end of the deposition the usual high temperatures were reached. All samples were completed to glass/Mo/CIGS/CdS/ZnO solar cells.

Thickness and composition of the CIGS layer were measured and evaluated. IV-analysis and Quantum efficiency measurements were carried out to characterize the solar cells. Additionally pictures of some samples were taken in the electron microscope.

Zusammenfassung

In dieser Arbeit wurde der Einfluss unterschiedlicher Substratemperaturprofile während der CIGS Beschichtung untersucht. CIGS wurde auf Mo beschichtete Substratgläser in einem In-line System coverdampft. Im Anschluss wurden komplette Solarzellen aus den Proben gefertigt und untersucht.

In drei Versuchsreihen wurde CIGS bei jeweils vier unterschiedlichen Substrattemperaturprofilen aufgedampft. In der ersten Versuchsreihe blieb die Temperatur während der Verdampfung weitgehend konstant. Es wurden Beschichtungen bei vier verschiedenen Substrattemperaturen durchgeführt. In den zwei weiteren Versuchsreihen wurde die Temperatur am Beginn der Deposition schrittweise verringert. Gegen Ende der Beschichtung wurden jedoch immer die üblichen hohen Substrattemperaturen erreicht. Aus allen Proben wurden Glas/Mo/CIGS/CdS/ZnO Solarzellen gefertigt.

Die Schichtdicke und die Zusammensetzung der abgeschiedenen CIGS Schichten wurde gemessen und ausgewertet. Von den Solarzellen wurden Strom - Spannungskennlinien aufgenommen und Quanteneffizienzmessungen durchgeführt. Zusätzlich wurden von einigen Proben Bilder im Elektronenmikroskop erstellt.

Contents

Chapter 1

Introduction

Globally growing demands for energy turn the spotlights on power supply making the development of new strategies and reliable sources for the future indispensible.

Apart from nuclear power, geothermal and tidal energy, all other energy sources are based on sunlight. Burning plants and their fossil remains (coal, oil and natural gas) have provided most of the energy up to now since fire was utilized by our ancestors. It is most evident that a further expansion of energy supply based on photosynthesis and fire would encounter major difficulties. Even the current level of combustion gives rise to serious worries about the side effects and the perpetuation of fuel supply.

Sunlight-based energy resources are tapped in many ways. Technologies like hydroelectricity, wind and wave generators have great potential and should not be underestimated. Nevertheless they account only for a relatively small fraction of the energy delivered by the sun. Only the direct use of sunlight opens the door to an almost endless source of energy, at least as regards the current consumer behaviour.

Thermal use of solar power is widespread and offers a direct use of sunlight in many different applications. Thermal solar power plants are an interesting approach for generating electricity, at least in a large scale generation.

Photovoltaic offers direct conversion of light to electricity. With efficiencies of more than 40 % [1] in laboratory cells it is the leading converter among all sunlight based electricity sources. It even outperforms many solar heating systems. The large variety of photovoltaic devices, from small calculators to large electricity plants makes it an almost universal source of energy. Clearly photovoltaic will play a prominent role in future energy supply.

As a result of intensified research activities and strategic support of commercialisation an extraordinary development of photovoltaic power generation has taken place in recent years. In Germany the contribution of photo-

voltaic will exceed 3 % of the total electricity generation in 2011 [2]. Similar rates are expected for Italy [3]. About 2 % share of Photovoltaic generation has also been reached in Spain and in the Czech Republic [4]. Most of the other countries are still far below these figures. Far stronger efforts are required for reaching a substantial contribution of photovoltaic to the energy supply in the near future.

From the large number of promising approaches regarding photovoltaic devices, only a few reached industrial module production yet. The properties of these more mature solar cells as well as their performance and history were reviewed some years ago [5].

Traditional silicon-based solar cells still dominate the market, though thin film technologies attract rising attention. Unlike crystalline silicon, direct gap materials are used as absorbers for thin film solar cells. The direct bandgap means that the lowest energy state in the conduction band and the highest state in the valence band have the same momentum. Therefore, light absorption is much stronger and only a few µm are sufficient for almost complete absorption. The very thin absorber layers stand for low material consumption and short energy payback times. Several technical advantages follow from thin film technologies. Monolithic integration allows for in-line production processes from the substrate to the finished module. Rapid roll-to-roll processes on flexible substrates translate into low-cost manufacturing.

So far three groups of thin film technologies have reached industrial production. Amorphous silicon (a-Si) has a long tradition on solar calculators and similar products. It was the first thin film technology to reach a significant market share. However, due to relatively low module conversion efficiencies the economic gain of the technology seems to be jeopardized.

Cadmium telluride (CdTe) modules have become the leading thin film technology in recent years. Although CdTe is a very stable non-toxic compound, the sheer involvement of cadmium fuels emotional debates.

The chalcopyrite absorber materials from the group I-III-VI$_2$ compound semiconductors provide bandgaps from 1.04 eV (CuInSe$_2$) up to about 3.4 eV in (CuAlS$_2$) [6], page 370ff. CIGS (Cu(InGa)Se$_2$)(Copper Indium Gallium Diselenide) reached the highest conversion efficiency within these materials. To translate its superior characteristics from scientific cells to commercial modules and industrial production, is still a challenge.

The highest efficiencies of CIGS solar cells so far have been achieved by co-evaporated CIGS layers. The substrate temperature during the co-evaporation process is in the focus of this work. Lower or partly reduced substrate temperatures save energy in the production process. In addition, a partly reduced substrate temperature might help to speed up production.

Usually the substrate temperature is kept constant during the deposition.

Constant temperatures help to improve reproducibility. Many investigations about different constant substrate temperatures have been published. In this work we varied the temperature during the deposition and analysed the effects of different substrate temperature profiles on CIGS formation and the resulting solar cells.

Chapter 2

Background

Conventional solar cells are based on the photoelectric effect in semiconductors. The photon energy lifts an electron from the valence band to the conduction band. The electric field of a pn-junction is needed to separate the generated hole from the excited electron in order to avoid recombination. The collected charge carriers provide a current to an external circuit.

In intrinsic semi conductors the number of free electrons equals the number of holes. This equilibrium can be changed for example by doping. The dominant charge carriers are called majority carriers. In a p-type material the holes are the majority carriers. Alternatively, if the electrons are the majority carriers the material is called n-type. A pn-junction is formed if the two different types of semiconductors are in contact. In homo-junctions p-type and n-type semiconductors are of the same material. For example a thin n-type layer on top of a p-type wafer is implemented by doping in crystalline silicon solar cells.

In the transition zone, holes diffuse into the n-type material and electrons into the p-type material. The resulting electric field drives back the charge carriers. A steady state is reached if the drift current caused by the electric field equals the diffusion current. This transition zone is called space charge region or depletion region and the electrical field herein allows for a charge carrier separation. In the case of a hetero-junction, two different semiconductor materials are combined to form a junction. The n-type material is usually a wide gap material aiming at avoiding light absorption before the light enters the depletion region. A photon can lift an electron from the valence band to the conduction band of a semiconductor if its energy at least equals the bandgap energy. The excited electron and the hole diffuse through the semiconductor. Only if the charge carriers enter the electric field of the space charge region, holes and electrons are separated and can be collected at a contact to provide current in an external circuit.

The photon spectrum of the sun closely follows the Planck distribution for a blackbody at 5800 K. The Carnot efficiency for a device at 300 K would be 95 %, but the maximum efficiency of a single bandgap solar cell is limited to about 30 %. Three main losses are responsible for the limitation of the theoretical efficiency. Firstly, all photons with energy below the bandgap energy cannot contribute. Secondly, the part of the photon energy above the bandgap is lost as the highly excited electrons quickly thermalize to low states in the conduction band. Even high energetic photons providing a multiple of the bandgap energy usually lift only one electron. Consequently the maximal number of electrons that contribute to the current of the device is limited to the number of photons with energy above the bandgap which are absorbed in the device. The third major loss is due to the fact that the output voltage of a solar cell does not reach the potential of the bandgap. The built in potential between the n and the p sides is always lower than the bandgap and the voltage is always lower than the built in potential. In practice the potential difference for the electron is between the conduction band edge on the n-side and the valence band edge on the p-side. A more detailed discussion can be found in textbooks like [6], page 71ff and references therein. Most efficiency calculations for semiconductor solar cells are based on the concept of Shockley and Queisser [7]. The ideal bandgap for terrestrial solar photovoltaics is at about 1.4 eV, but good conversion efficiencies are possible from 1 eV to 1.7 eV.

Many ideas and concepts have been developed to get around this limit. An interesting overview is given by Martin Green [8]. The most obvious way to enhance the efficiency are multi-junctions with decreasing bandgaps from top to bottom. Indeed impressive results under concentrated light have been shown, with conversion efficiencies above 40 %. The latest solar cell efficiency tables provide a picture of the best results achieved within different technologies [1].

The natural solar spectrum on earth reflects the absorption in the atmosphere. Obviously the weather strongly influences the intensity of the light. For example in central Europe the average yearly solar radiation is dominated by diffuse light, which has been reflected by clouds, fog or the ambiance. As the sun approaches the horizon the way through the atmosphere grows and less light arrives on the earths surface. For measurements of solar cells the AM1.5 standard spectrum is defined. It corresponds to light that travelled from the sun to the earth through 1.5 times the thickness of the atmosphere. The overall intensity is 1000 W/m^2 and standard test conditions refer to a cell temperature of 25 °C.

2.1 Basic characteristics and analysis

The simplest model for the current voltage characteristic of a solar cell is Shockleys ideal diode equation 2.1. When the voltage vanishes follows from this equation, that the short circuit current, I_{sc}, is the negative photo current. On the other hand the open circuit situation, which corresponds to vanishing current leads to an expression for the V_{oc}, the maximal open circuit voltage [7].

$$I = I_0\left(e^{\left(\frac{qV}{kT}\right)} - 1\right) - I_{ph} \tag{2.1}$$

$$V_{oc} = \frac{kT}{q} \ln\left[\left(\frac{I_{ph}}{I_0}\right) + 1\right] \tag{2.2}$$

I...	current	I_0...	dark saturation current
q...	electron charge	V...	voltage
k...	Boltzman constant	T...	absolute temperature
I_{ph}...	photo current	V_{oc}...	open circuit voltage

However in a real device a series resistance is unavoidable. In addition the cell is not a perfect isolator but has a finite shunt resistance, called parallel resistance. This can be taken into account by introducing additional terms for voltage and current. This leads to equation 2.3. The ideality factor in the diode equation allows to consider deviations from the ideal behaviour. Taking into account recombination in the depletion region motivates the two diode model in equation 2.4. The theoretical value for the ideality factor in the second diode is two, as compared to one for the first.

$$I = I_0\left[e^{\left(\frac{q(V-R_sI)}{AkT}\right)} - 1\right] + \frac{V - R_sI}{R_p} - I_{ph} \tag{2.3}$$

$$I = I_{01}\left[e^{\left(\frac{q(V-R_sI)}{A_1kT}\right)} - 1\right] + I_{02}\left[e^{\left(\frac{q(V-R_sI)}{A_2kT}\right)} - 1\right] + \frac{V - R_sI}{R_p} - I_{ph} \tag{2.4}$$

A, A_1, A_2,...	ideality factor	R_s...	series resistance
R_p...	parallel resistance	I_{01},I_{02}...	dark saturation current

The product of current and voltage represents the power of the solar cell, its maximum is called the maximum power point. The ratio of the maximum
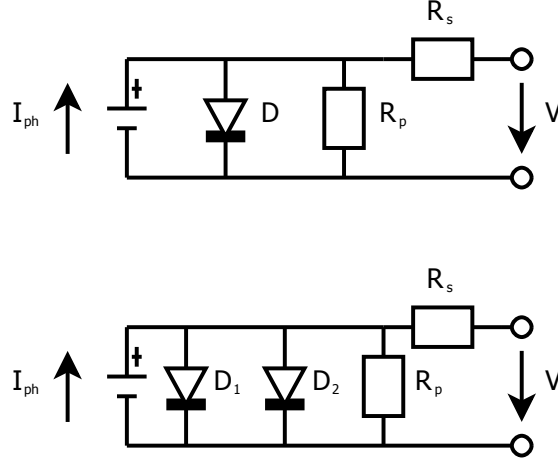
Figure 2.1: Equivalent circuit diagram of the one and two diode model

power to the product of short circuit current and open circuit voltage is the fill factor. Conversion efficiency, or shortly efficiency of a photovoltaic device is the ratio of electric power to incident light power. It depends not only on the device and its temperature but also on the light spectrum. As mentioned above the usual standard for terrestrial applications is the AM1.5 spectrum.

$$FF = \frac{P_{MPP}}{I_{sc} \times V_{oc}} = \frac{I_{MPP} \times V_{MPP}}{I_{sc} \times V_{oc}} \tag{2.5}$$

$$\eta = \frac{P_{MPP}}{P_{light}} = \frac{I_{MPP} \times V_{MPP}}{P_{light}} = \frac{FF \times I_{sc} \times V_{oc}}{P_{light}} \tag{2.6}$$

FF...	fill factor	P_{MPP}...	maximal power
I_{sc}...	short circuit current	V_{oc}...	open circuit voltage
I_{MPP}...	maximal power point current	V_{MPP}...	maximal power point poltage
P_{light}...	illumination power on the cell		

Current voltage characteristics are carried out with IV measurement se-tups. The device is illuminated with a calibrated light source. The cell is connected to a voltage source and an ampere meter. For each voltage value the current is measured, resulting in an IV-curve. I_{sc}, V_{oc} and P_{MPP} are
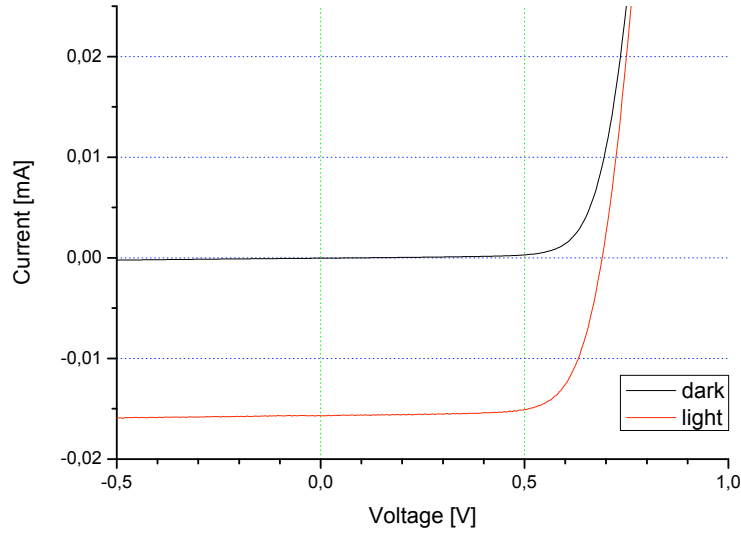
Figure 2.2: Light and dark IV-curve of a CIGS solar cell. The cell was produced in the preliminary phase for the temperature grading experiments.

measured and fill factor and efficiency can be directly calculated from the results. Values for the diode ideality factor series- and parallel- resistance can be obtained by fitting the results. In figure 2.2 the measured IV-curve of a high efficient (16.2 %) CIGS solar cell is shown. Further IV-curves of selected cells are plotted in figures 6.5 to 6.7 in chapter 6.

The spectral response or quantum efficiency of a solar cell represents its ability to convert photons of different energy into electric current. The external quantum efficiency is the ratio of incident photons to electrons available at the cells contacts to an external electric circuit.

$$J_{ph} = q \int_{0}^{+\infty} \eta_{q(\lambda)} \rho_{ph(\lambda)} d\lambda \tag{2.7}$$

J_{ph}...	photo current density	$\eta_{q(\lambda)}$...	External Quantum Efficiency
$\rho_{ph(\lambda)}$...	photon flux density	λ...	wavelength

To measure External Quantum Efficiency (EQE) a calibrated light beam for each wavelength is needed. The induced photo current is measured in a
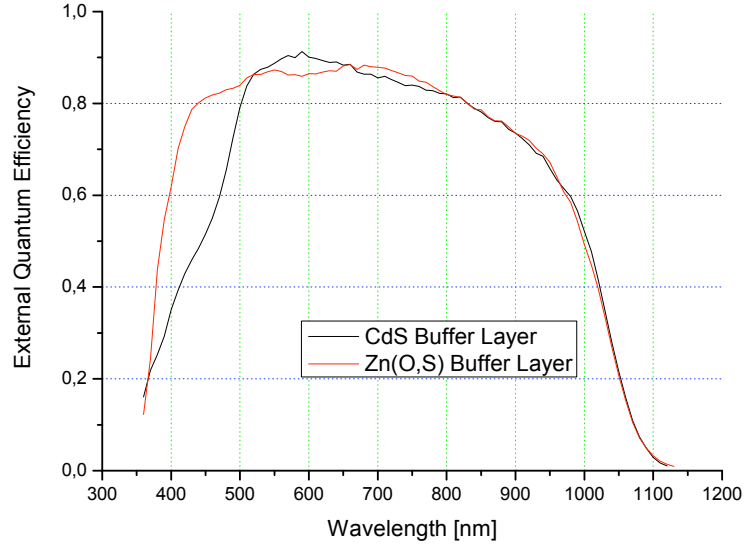
Figure 2.3:   External Quantum Efficiency (EQE) of two CIGS solar cells with different buffer layers. The Current-Voltage characteristic of the cell with a CdS buffer layer is shown in figure 2.2. It shows comparable weak performance at short wavelengths below 500 nm. This decline of the EQE is due to absorption in the CdS layer. Both cells are the result of preliminary experiments.

short circuit situation. With equation 2.7 the photo current for any spectrum of interest can be calculated from the EQE results. As an example in figure 2.3 the external quantum efficiency of two CIGS solar cells with different buffer layers is presented. Additional EQE-curves of selected cells are plotted in figures 6.8 to 6.10 in chapter 6.

2.2   Chalcopyrite

The interest in Chalcopyrite I-III-VI$_2$ compounds emerged from promising results with CuInSe$_2$ single crystalline solar cells [9, 10]. The $(Cu(In, Ga, Al)(S, Se)_2)$ alloy system became a playground for photovoltaic research. The group III elements Ga and Al can be replace In in arbitrary amounts. In a similar way Se can be replaced by S. The wide bandgap range available within these alloys opens a large field of applications and research. First successes in thin

film deposition and thin film devices were soon reported [11, 12]. $CuInSe_2$ was the first thin film absorber reaching cell efficiencies above 10% in the early 1980s.

Partly replacing In with Ga leads to CIGS ($Cu(In_{1-x}Ga_x)Se_2$). The abbreviation CIGS is very common but sometimes misleading. The S here stands for Selenium and should not be mistaken for Sulfur. The addition of Ga leads to an increase of the bandgap. It turned out that for small amounts of Ga up to x=0.4, the photovoltaic characteristics of the material improve strongly, not only due to the increased bandgap. Improved photovoltaic performance was also reported when adding small amounts of Ga to $CuInS_2$. Though in this case a bandgap growth is not convenient [13].

The best thin film solar cells reported in the last decades are based on coevaporated CIGS in a layer construction which has become a standard for chalcopyrite thin film solar cells. This structure will be presented in the following section. Recently efficiencies exceeding 20% have been reported [1]. Additional to CIGS, high efficiencies have been reported also for $(Cu(In, Al)Se_2)$ and $(CuInSe_2)$[14, 15].

2.2.1 Standard CIGS solar cell structure

Thin film solar cells consist of several layers denominated by their functions as substrate, back contact, absorber, buffer layer for the hetero junction, and a (transparent) front contact, additionally in the case of single cells a metallic grid on top can enhance the carrier collection.

SLG (Soda Lime Glass) is the most common substrate. A sputtered Mo layer provides the ohmic back contact to the absorber. Substrate and back contact need a thermal expansion coefficient similar to the absorber material to avoid mechanical stress and delamination. Absorber deposition by thermal coevaporation yields the best photovoltaic results, but alternatives are intensively investigated. The pn hetero-junction is formed by depositing a n-type semiconductor layer directly on the p-type absorber. CdS formed in CBD (Chemical Bath Deposition) is the conventional n-type buffer layer. Usually ZnO:Al (Al doped ZnO) is used as front contact but a very thin layer of intrinsic ZnO (highly resistive) improves the band alignment to the CdS, isolates shunt paths and is evidently crucial to achieve good results in this structure.

A wide gap buffer material is required to avoid undesired absorption in the buffer layer. Alternatives to CdS are explored for several reasons, to avoid toxic Cd, to get around the CBD procedure in a series of vacuum processes and to improve performance by using a material with a wider bandgap. Though promising results have been published, CBD CdS is a widely used

standard and serves as a reference for alternative buffer layers. The Graph in figure 2.3 shows the effect of the optical absorption in the CdS on the EQE. This absorption is responsible for the weak performance at wavelengths below 500 nm, typical for CIGS cells with a CdS buffer layer.

In modules the front contact is used for monolithic interconnection, while in research small isolated cells are provided with a metallic grid to enhance carrier collection and to facilitate measurements.

The above described structure is presented in textbooks like [6]. It has been first developed for CuInSe$_2$ based cells, reported for example in [15, 16]. Surface and interface properties are of great importance for multilayer devices. The electronic characteristics of CIGS and the above discussed structure have been intensively explored. U. Rau and H. Schock presented a detailed review about the electronic properties of CIGS [17].

2.2.2   Co-evaporated CIGS

Simultaneous Co-evaporation of four different materials remains a tricky process, but due to its outstanding solar cell results it is nevertheless used by some manufacturers in CIGS production. The vapour pressure is very sensitive to temperature, hence only precise control of the source temperatures leads to control of the evaporation rates and thereby control of the composition of the deposited material and reproducible results. This is important for the sources for the metals Cu, In and Ga. The situation is somewhat different for Se, which is always evaporated in excess as compared to the evaporation rate necessary to reach stoichiometry in theory.

Basic concepts of semiconductor physics are applied to describe photovoltaic devices. In the case of elemental single crystal materials relatively simple models of ideal crystals are quite close to reality. The situation is somewhat different in multi crystalline thin film compound semiconductors. Theoretical models so far offer only limited help for a detailed understanding of the electronic properties of CIGS films. Though CIGS is far away from being fully understood, a remarkable body of knowledge was put together in various research groups. In a recent review 'The electronic structure of chalcopyrites-bands, point defects and grain boundaries' the matter is presented [18].

Some guidelines can be formulated for deposition of device quality CIGS by coevaportion.

Though a Cu rich state during deposition is considered helpful for crystal formation, the overall composition needs to be Cu poor. High Cu contents are critical as a secondary phase of Cu-Se is formed near and above stoichiometric copper contents. This additional phase is degenerated p-type, and it strongly

rises the conductivity of the material. The Cu-Se phase segregates on the materials surface. The photovoltaic characteristics are severely effected by this secondary phase [19]. To achieve device quality CIGS, Cu excess in the overall composition has to be avoided. The best results are usually obtained at an overall Cu/(In+Ga) ratio of 0.8 to 0.9.

Device performance rises with Ga content up to a Ga/In ratio of 0.3 to 0.4. Higher Ga contents would be desirable to optimise the bandgap, but the photovoltaic properties of CIGS suffer at higher Ga contents.

Se evaporates in rings or chains of atoms. These relatively large molecules show low reactivity and low adsorption at high substrate temperatures. The CIGS deposition takes place under Se overpressure in a Se athmosphere. Low Se rates inhibit the formation of device quality CIGS, while high rates are not so critical, but raise Se consumption. To avoid Se vacancies in the surface region, the cool down phase after deposition starts in a Se atmosphere, however the deposition of Se on the surface is undesirable. An investigation for a three stage process is presented in [20].

The reactivity of the evaporated Se can be enhanced if the rings or chains are cracked to elemental Se or small reactive Se clusters. This can be achieved by additional heating after evaporating or cracking in an electric radio frequency field. This technique could avoid the unfavourable high consumption of Se in production processes. A second advantage could be improved CIGS formation, specially at lower substrate temperatures and high deposition rates [21, 22, 23, 24].

The best results are achieved on SLG substrates at high deposition temperatures near the softening point of SLG at about $550\,^{\circ}\text{C}$. SLG is important because the 'natural' indiffusion from of Na from SLG into the CIGS layer is responsible for the outstanding device results. Both matters will be discussed in the following subsections.

Sodium in CIGS

SLG, which is the same as common window glass, has become the favourite substrate material because it releases sodium (Na) to the CIGS at high process temperatures near the softening point of SLG at about $550\,^{\circ}\text{C}$. Though at first unexpected, Na indiffusion from the substrate through the back contact into the CIGS absorber, was found to be responsible for the functional outperformance of SLG based solar cells, as compared to any other substrate.

The effects of sodium have positive influence on structural and electric properties of chalcopyrite absorbers. This was reported for coevaporated $CuInSe_2$ absorbers [25] and turned out to be similar for CIGS. The positive effects of Na are evident, why and how Na acts during deposition and in the

material remains still a subject of the scientific debate. A current report was published by Ishizuka et al [26].

The most important impacts of Na in CIGS are specified in the following list. Most effects are dicussed by Ishizuka in the above mentioned article, but can also be found in textbooks like [27].

- The interdiffusion of Na in CIGS takes place mainly along grain boundaries.

- Passivation of unavoidable surface defects, in particular Cu vacancies at grain boundaries.

- Increase in the hole carrier density and thereby enhanced p-type conductivity.

- Increased V_{oc} and Fill Factor.

- Decrease of elemental interdiffusion.

- Expansion of the existence range of the chalcopyrite α-phase. [28]

Control of Na diffusion through the Mo layer is quite difficult. Very dense Mo can be a Na barrier, but the possibilities to actively control the Na diffusion by changing the Mo deposition parameters are limited. Several alternative Na sources have been developed and are in use for deposition on different kinds of Na free substrates. For example alkaline precursors and coevaporation [29] or silicate thin layers [30, 31]. Good results have been reported with efficiencies above 17 % on different substrates. The latest highlight was reported by Chirilă et al. on a flexible polyimide substrate at relatively low substrate temperature in a 'modified three stage process' with a cell efficiency of 18.7 % [32]. Despite all efforts the 'natural' indiffusion from SLG substrates into the CIGS layer in combination with the 'three stage process' still yields the best solar cells.

The three stage process and composition control

The simultaneous control of several sources becomes more complicated with each additional source because their behaviour is not independent. Many of the techniques in CIGS deposition emerged from $CuInSe_2$ deposition. This explains why Ga is often treated only as a partly substitution of In, eg. as an extension of the $CuInSe_2$ system.

One option to reduce complexity is to coevaporate not all materials at the same time. The usual approach is to keep the Se source running at a constant

high evaporation rate and to vary the rates of Cu and (In+Ga). The most sucessful is the so called 'three stage process which was first published by Gabor et al. [33]. This deposition technique has become almost a standard in stationary or batch CIGS coevaporation.

The three stage process starts with the deposition of In and Ga. In the second step Cu is evaporated and in the last step again In and Ga. In the second stage a Cu rich overall composition is reached and a 'liquid' Cu_xSe phase is reported to assist recrystallization [19]. In the last stage the desired Cu poor overall composition is reached again. The optical and electrical properties of Cu rich CIGS are different as compared to the Cu poor material. This was found to be useful in composition monitoring [34, 35]. The change in the emissivity of the material at the transition from Cu poor to Cu rich changes the thermal balance. If the substrates are kept at constant temperature a change in heating power signals the transition point, alternatively if the substrates are heated with constant power, a change in the substrate temperature marks the stoichiometric composition.

In the first step In and Ga are deposited at low substrate temperatures (300 °C to 450 °C). While the substrate temperature is kept near the softening point of glass in the other two stages. The three stage process is a common technique in many research groups with some variations, and is common for alternative substrates too. However the process may be inappropriate for high throughput in production since it is difficult to implement in an in line system and the recrystallisation limits the possibilities to speed up deposition.

Radiation based in situ monitoring of film thickness and composition has been reported in several papers [36, 37, 38]. A powerful method is 'mass spectrometer feed-back control of the metal evaporation' [39]. This approach allows for real time monitoring and for realising desired rate profiles in an automatic mode. The system is very helpful to imitate in line processes.

The above presented monitoring techniques are important for process control in batch processes, but are difficult to implement in a steady state in line system like it was used for this work. The body of acquired knowledge however provided the basis to design and run powerful inline systems.

The steady state in line approach relies on stable sources, the rates are constant and the substrates continuously pass by. A precise control of the source temperatures is of central importance to control evaporation rates and to reach high reproducibility. The composition and thickness of the CIGS layer are quantified only once the substrates are taken out. In exchange for flexibility the in line system has the capacity to provide large quantities of high quality samples for intense studies of buffer and window layers as well as for mini module research. Furthermore the results and experience are

valuable for large scale production.

2.2.3   Substrate Temperature

CIGS is a very stable compound with a melting temperature between $987\,°C$ ($CuInSe_2$) and $1060\,°C$ ($CuGaSe_2$), depending on the composition. Coevaporation of CIGS requires high substrate temperatures if large grains are desired. On SLG the substrate temperature is limited at about $550\,°C$ due to softening of the glass.

Lower substrate temperatures permit to reduce heating energy and to avoid glass bending. Deposition temperatures of $420\,°C$ or less would allow to use alternative substrates like polyimide.

The substrate temperature has several effects on the CIGS layer. On colder substrates nucleation is faster, the surface is quickly covered by small 'islands'. The same trend is reported for higher deposition rates [40]. In this work we had very high average deposition rates of about $2\,nm/s$. However due to the geometry of our system the rates are lower in the beginning and the end of the deposition and the composition of the flux changes during deposition. Grain growth of deposited material is a relatively slow process and requires high temperature [41]. The grain size decreases at lower substrate temperatures.

The most important effect for the device quality on SLG substrates is Na diffusion which is reported to be strongly temperature dependent. At lower substrate temperature alternative Na sources can be used to avoid performance loss due to a lack of Na. It is a common method to add Na, when Na free substrates are used. Positive effects of additional Na are reported for different processes at low substrate temperatures [29, 42, 43].

It can be summarized that down to substrate temperatures of $400\,°C$ highly efficient CIGS has been shown to be possible. Below $400\,°C$ not only small crystals are reported but also poor electrical characteristics. Recent surveys of substrate temperature effects have been published for multi stage processes [44] and for a one stage process [45].

Chapter 3

Experimental details

3.1 Preparation

For the experiments in this thesis SLG substrates were used. The size of the substrates used, is $12.5\,cm \times 12.5\,cm$ at a thickness of $2\,mm$. Properly cleaned substrates are of great importance for reasonable results and reproducibility.

Carefully carrying out the following description of the washing procedure is an important first step. After numbering, the glasses are cleaned in a series of ultrasonic baths in de-ionized water. A detergent is added to the first bath and between the baths the glasses are continously rinsed in de-ionized water. From the last bath the substrates are directly moved into a spin dryer with nitrogen atmosphere. The dry and clean substrates are stored in dry nitrogen atmosphere.

3.2 Sputter system MRCII

The MRCII is a semi automatic vertical inline DC magnetron sputter system from the Materials Research Corporation, Typ 603. The substrates are mounted on a platform which is shown in figure 3.1. A carrier leads the platform past the sputter targets, the carrier speed determines the thickness of the deposited layer. Three different sputter targets are usually mounted in the MRCII: Mo, i-ZnO, Al:ZnO. The system allows a maximum substrate size of $30\,cm \times 30\,cm$, which makes it possible to coat up to four of our $12.5\,cm \times 12.5\,cm$ substrates in one run. The MRCII was used for the Mo back contact, the i:ZnO window layer and the Al:ZnO front contact of the solar cells in this project. Sputter parameters, thickness and conductivity of the layers are given in table 3.1 on page 25.
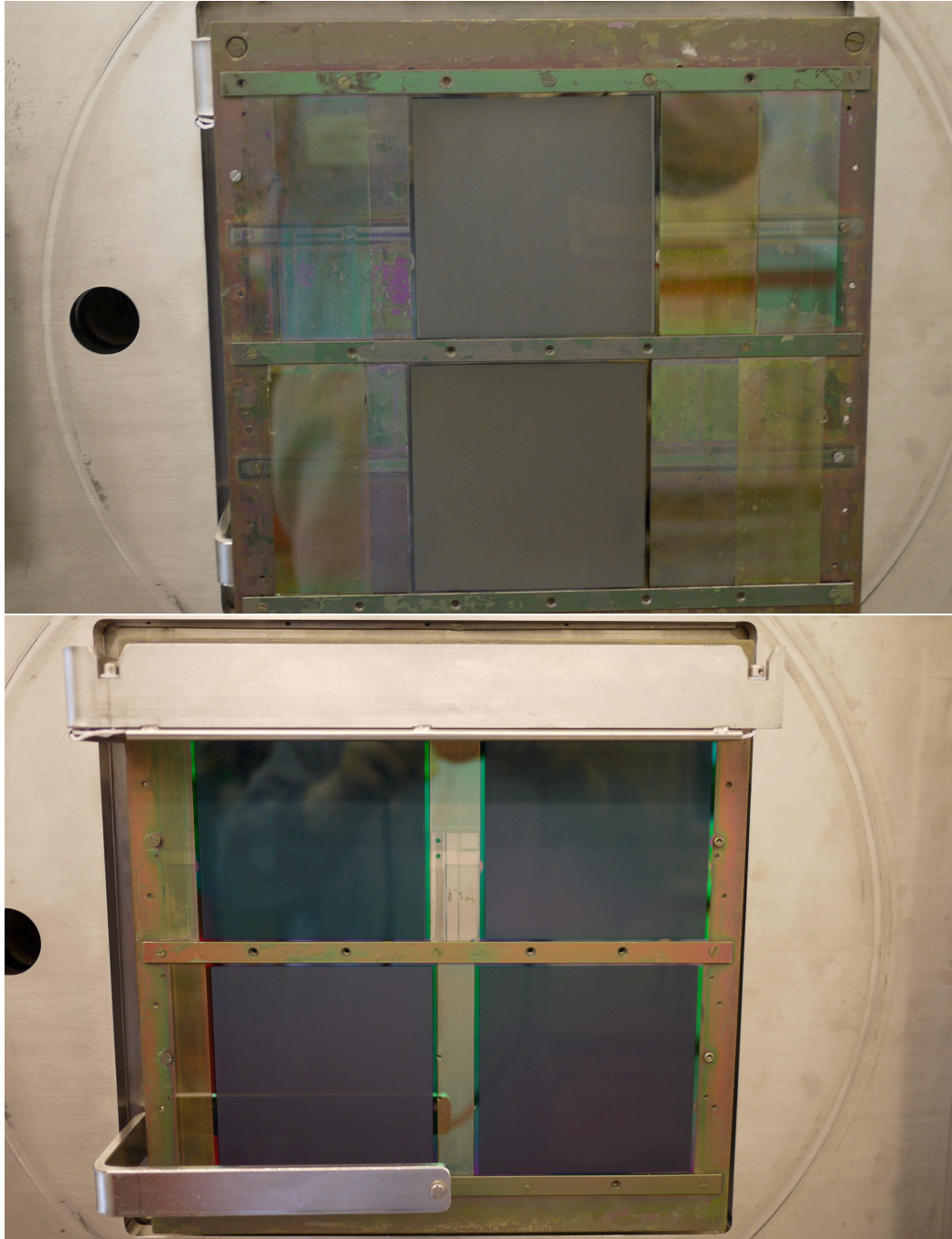
Figure 3.1: The MRCII's loadlock
Top: SLG/Mo/CIGS/Zn(O,S) substrates loaded on a platform;
Bottom: Freshly ZnO coated SLG/Mo/CIGS/Zn(O,S) substrates on a platform

3.3 Buffer layer: ALD / Bath

The standard buffer layer for CIGS is CdS which is commonly deposited in a chemical bath. Of the two samples coated with CIGS in each run we supplied one with CdS and the second with Zn(O,S) as an alternative buffer layer.

For the chemical bath 13 ml concentrated ammonia solution NH_4OH (Ammonium hydroxide) are diluted with de-ionized water to a solution of 100 ml. 0.13 g $Cd(CH_3CO_2)_2$ (Cadmium acetate) and 1.33 g $SC(NH_2)_2$ (thiouria) are seperately disolved in de-ionized water. The resulting 50 ml Thiourea solution, the 25 ml Cadmium acetate solution and the ammonium hydroxide solution are filled in a beaker and mixed. The samples are added. In a $60\,^\circ C$ water bath the beaker is heated for 8 min, during this time CdS is formed. The resulting layer of about 50 nm covers all solids in contact with the liquid.

The process chamber for the ALD (Atomic Layer Deposition) was designed in the research group. A detailed description can be found in [46]. DEZn (Diethylzinc, $(C_2H_5)_2Zn$) and H_2O are used as precurser gases and N2 (Nitrogen) to wash out the excess gas. In every 7th cycle H_2O is replaced by H_2S(Hydrogen Sulphide). After 70 cycles a $Zn(O,S)$ layer of about 20 nm is built.

3.4 Grid: Electron beam evaporation, Scribing

Two different vacuum systems were used to provide the cells with a bimetallic Ni-Al-Ni triple layer. One is a Balzer system Typ: BA 510 A, the other

Table 3.1: MRCII Sputter Parameter

Parameter	Unit	Mo	ZnO	Al:ZnO
h base pressure	[Pa]	$< 10^{-4}$	$< 10^{-4}$	-
sputter power	[W]	1500	600	1500
gas pressure	[Pa]	0.8	1.6	0.4
carrier speed	[cm/ min]	6	12	3
frequency	[kHz]	-	150	100
pulse time	[µs]	-	2.9	4.5
sheet resistance	[$\Omega\square$]	< 1	-	≈ 50
thickness	[nm]	200	50	400

Figure 3.2: Liquid Al source heated by the electron beam

one, named Flutter, is a design of Uppsala Universiy. Both systems are electron beam evaporators using a cryo-pump system. In the Balzer system the sources are mounted on a turntable. With one electron gun different materials can be evaporated without opening the system. In Flutter two sources and two electron guns are available. The Al source in the Balzer system can be seen in figure 3.2.

Metal masks are used to define the shape of the grid and the size of the cells. The masks for the standard cells are $10 \, cm \times 10 \, cm$ large and are designed for $0.5 \, cm^2$ cells with two grid fingers.

In a last step a mechanical scriber draws the border of the cells. In this process the Mo back contact remains but the CIGS and the layers on top of it are removed in form of a trench around the cell.

3.5 The micro-pilote deposition System MP

3.5.1 The system

The cylindrical vacuum system, shown in figure 3.3, used for the coevaporation of CIGS is called Monsieur Pilote or shortly MP. The micro-pilote system was designed to simulate an inline CIGS production. Dr. John Kessler from France, a former member of the group, called the system Monsieur Pilote. He was responsible for the original setup and manufacturing of the machine, which was produced by Von Ardenne.

The main vacuum chamber has the shape of a cylinder. The four sources for Copper, Indium, Gallium and Selenium are in a box in the center of the cylinder which is open towards the evaporation zone. The substrate holders hang from a turntable, so the vertically orientated substrates are covered with a CIGS layer on the inside and heated from the other side where the substrate heaters are mounted near the chamber wall.

Two big turbo vacuum pumps are mounted for pumping the main vacuum chamber and one small pump for each of the three loadlocks. On the racks in the loadlocks up to 24 substrates can be loaded. A robot arm takes the substrates from the rack and puts them on the turntable positions in the main chamber. In this way 24 samples can be processed automatically in one session. The turntable has 24 substrate positions which are all filled with so called dummy substrates to prevent the heaters from being exposed to the evaporation. Whenever a fresh substrate is put in, the dummy or substrate from the desired position needs to be taken out first.

Figure 3.3: **The MP vaccuum chamber with open lid.**
On the turntable the dummy-substrate backsides behave like mirrors. In the left bottom corner the two pyrometers are mounted. Inside the chamber in the center is the metal box that hides the sources, on its left the metal cool down curves are visible. In the back is the opening located through which the substrates come and go.

3.5.2 Roundtrip

In a virtual journey we accompany a substrate traveling one circle in the MP to get a better idea of the system. The schematic drawing on page 29 helps to understand the system configuration.

The robot arm puts the substrate in one of the 24 substrate positions, The door is locked behind it and the molybdenum coated substrate surface faces

the box that contains the sources. The substrate is exposed to a selenium atmosphere at about 10×10^{-5} bar in the chamber. The turntable starts rotating. At an angle of 15°, the substrate is moved one position further and meets the first of 14 substrate heaters. Each substrate heater contains six halogen lamps and corresponds to a position equivalent to 15°. The first six heaters build the warm up zone. In the sixth heater a thermocouple is mounted, which will be referred to as thermocouple 6 (TH6) due to its position. Here, on the other side of the substrate is a thermocouple inside, therefore called TH6i. TH6 can be used to control the heaters in the warm up zone.

When heater seven is reached the substrate enters the evaporation zone. From heater six to heater 14, thermocouples are mounted between the heaters to monitor the substrate temperature. These thermocouples are called (TH6.5, TH7.5, ... , TH13.5) according to their position. The substrate now directly faces the three metal sources and the deposition of CIGS takes place. The hot sources, their temperatures are listed in table 3.2 on page 30, now additionally heat the substrates. At heater 11 and 12 the substrate passes the two pyrometers which are mounted outside and measure the substrate temperature on the backside through a view port. In heater 13 an additional thermocouple (TH13) is mounted like in heater six. With the end of heater 13 the evaporation zone ends.

Now the substrate is still heated from the back, but it already starts to cool down. From here to the loadlock the substrate travels through the cooling zone, two water cooled metal curves in the front and the back. After about one hour the substrate reaches the lock again, is taken out and stored in one of the loadlocks.

3.5.3   Restart

The MP system proved to be a powerful instrument after it was built more than ten years ago. It marks the starting point of a successful commercialisation of the process and provided the CIGS layer for outstanding scientific work. Cell efficiencies up to 18.5 % [46], with anti reflection coating, have been shown for $Zn(O, S)$ buffer layers and 18.1 % for $(Zn, Mg)O$ buffer layers [47].

Due to a short-circuit in one of the sources the system paused when I started my work and needed a major revision. It was my first task to restart the MP together with Dr. Uwe Zimmermann who was responsible for the project.

The heart of the system, the metal sources had to be renewed completely. We mounted the new sources, new, stronger vacuum feedthroughs and con-
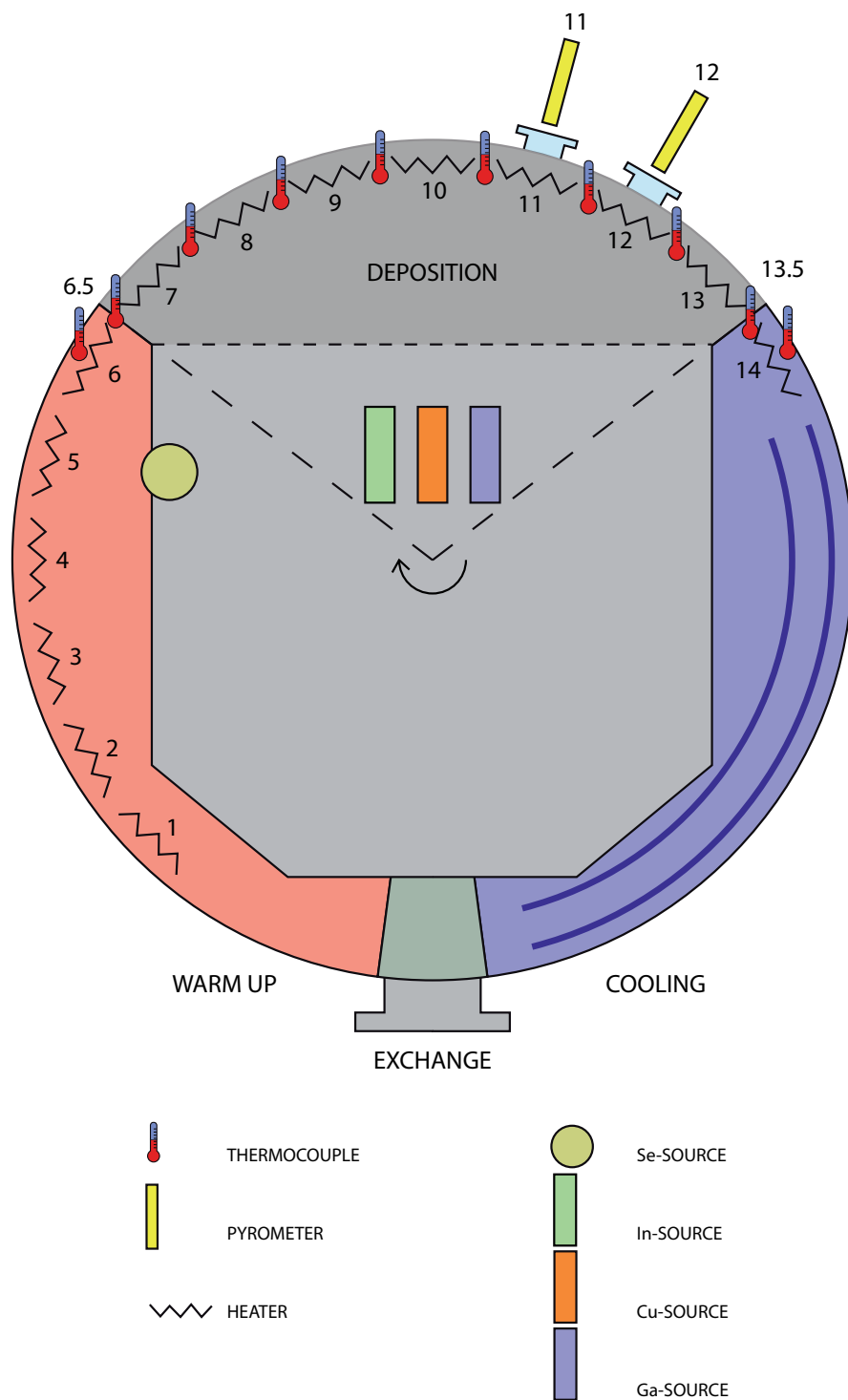
Figure 3.4: MP schema

Table 3.2: Temperatures of the sources in the MP, the assigned error refers to the stability of the sources.

Cu_{base}	1370 °C	+- 1 °C
In_{base}	1035 °C	+- 1 °C
Ga_{base}	1130 °C	+- 1 °C
Se	265 °C	+- 1 °C

nected the sources to new DC-powersupplies. The three metal sources consist of pyrolytic boron nitride crucibles. The cylindrical crucibles are mounted horizontally and heated from the outside by filament heaters. The metal sources have two independent heaters one for the base and one for the tip. To minimize radiation losses the heaters are covered with multilayer metal heat shields. The temperatures are controlled by a thermocouple in connection with a EUROTHERM® control unit. As the source temperatures are very stable the evaporation rates can be precisely controlled. For all CIGS runs in this project we used the same source temperatures. Due to the high stability and quality of the sources we always had the same evaporation rates. The six power supplies have individual current and voltage limits to prevent major short-circuit catastrophies.

Additionally we replaced all thermocouple extension wires and introduced TH6i and tuneable resistors to allow individual control of heaters 7 - 12. Finally we realized a new data logging system for all available data in the MP.

After the restart, the MP turned out to be very stable and to deliver reproduceable results. We could not reach former records but found a recipe that led to cell efficiencies above 16 % without anti reflection coating. The settings for the sources are plotted in table 3.2 on page 30 and were used for all MP runs in this project.

3.5.4   Post deposition heating

In the first runs after the restart of the MP we observed poor results with CdS buffer layers, while Zn(O,S) buffer layers showed promising efficiencies up to 16 %. Similar device results have been seen in connection with surface Se on the CIGS layer. The influence of elemental Se has been investigated in previous studies at the Ångström Solar Center [48]. Diffractive x-ray analysis

showed elemental Se on the Surface of the CIGS layer. To avoid surface Se we introduced a post deposition heating step. Without starting the sources, the substrates were heated up to a temperature of about 330 °C in the MP.

The efficiency of CdS-buffer layer solar cells improved strongly with this step. All solar cells for this project have been heat treated as described above.

Chapter 4

Temperature measurements

In principle all temperature dependent material properties can be used to measure temperatures. Of the huge variety of thermometers, only two are brought in to measure temperatures in MP and will be introduced in this chapter. Thermocouples control the substrate heaters, the source temperatures and track the substrate temperature during deposition. Two pyrometers measure the absolute temperature of the substrates.

4.1   Thermocouples

Thermocouples make use of the thermoelectrical effect to measure temperatures. In 1821 Thomas Seebeck discovered that a circuit of two dissimilar metals deflects a compass needle when the two junctions have different temperatures. What Thomas Seebeck called the thermomagnetic effect was found to result from the fact that a temperature gradient in conductors and semiconductors gives rise to an electric field. In so called normal metals, where the electrons are well described by the concept of free electrons, the electrons accumulate in the cold part, as the higher energy of the warm electrons enables them to travel faster. The potential difference between the hot and the cold region depends on the heated metal and is gauged by the Seebeck coefficient S. S is negative for normal metals and in the order of microvolt per °C. Parameters like electron density, mean scattering time and effective electron mass depend on the temperature and might force the electrons to accumulate in the warm region like in Cu or Mo, which therefore have a positive Seebeck coefficient. Within a circuit of only one metal the effect cancels out for symmetry reasons. A junction of two dissimilar metals is called a thermocouple. A current flows in a circuit with two thermocouples when they are at different temperatures. If the circuit is open a voltage can

be measured. To measure temperatures one thermocouple has to be held at a constant reference temperature, this is called the cold junction, while the other thermocouple at the temperature to be measured is the hot junction. As standard reference temperature the ice point at $0\,°C$ is used. Voltage values for thermocouples are found in tables. However in a real measurement setup the cold junction is the connection to the Voltmeter, both terminals are carefully held at the same temperature which is measured by a thermistor. The temperature difference of the cold junction to $0\,°C$ has to be considered. If this is done by calculations of the instrument it is called software compensation. In MP Type C thermocouples (WRh5/WRh26) are used to measure the metal source temperatures. Type K thermocouples (NiCr10/NiMn2Al2Si1) are used to measure the Se source and the substrate temperatures.

Table 4.1 shows the IEC (International Electrotechnical Commission) standard thermocouple types. The data is taken from [49] where the matter of thermocouples is described starting at page 119. The temperature range follows from the IEC 584-1 thermocouple tables tolerance classes. The type letters in the table are linked to NIST (National Institute of Standards and Technology) reference tables of the thermal voltage. The data for type C thermocouples are from [50] where practical information and tables are available. All links are printed in the appendix.

Table 4.1: Standard Thermocouples

Type	composition	min. temp.	max. temp.
		[°C]	[°C]
T	Cu-CuNi45	-200	350
J	Fe-CuNi45	-40	750
E	NiCr10-CuNi45	-200	900
K	NiCr10-Ni	-200	1200
N	NiCr10-Ni	-200	1200
R	Pt13Rh-Pti	0	1600
S	Pt10Rh-Pt	0	1600
B	Pt30Rh-Pt6Rh	600	1700
C	W5Re-W26Re	425	2320

Figure 4.1: MP: Heaters 8 to 12 and Thermocouples TH8.5 to TH11.5. In heater 11 the hole in the middle through which pyrometer 11 detects the radiation from outside is visible.

4.2 Pyrometer

Pyrometers directly measure the radiation of the desired object and translate it to temperature according to Plancks Law. For a black body absolute temperature follows upon measuring the intensity at one wavelength. The pyrometers used in MP measure the intensity at a wavelength of 5.3 µm at which the thermal emissivity of glass reaches 0.97. i.e. very close to one. The setting of the pyrometer to consider different emissivities is set to one. The design and setup of the pyrometer temperature measurement in MP is the scope of a previous diploma project [51]. In this work the general difficulties and advantages of radiative temperature measurements and the special situation in MP are carefully discussed.

The MgF_2 view port has an optical transmittance of 97 % [52] at wavelength of 5.3 µm. The view port reduces the effective emissivity to 0.94, which would be the ideal setting for the pyrometer.

The deviation of the measured value from the true temperature caused by reduced emissivity can be calculated. The matter is discussed in [49] on page 176 and 177. A relation between the object temperature and the temperature measured by the pyrometer is given by equation 4.1 from [49] page 176. The difference between the two values is a systematic error. The deviation depends on the operating wavelength of the pyrometer and on the temperature measured. Equation 4.2 follows directly from equation 4.1. With this tool we can directly calculate the systematic error. In figure 4.2 the temperature difference is plotted for various effective emissivities. All
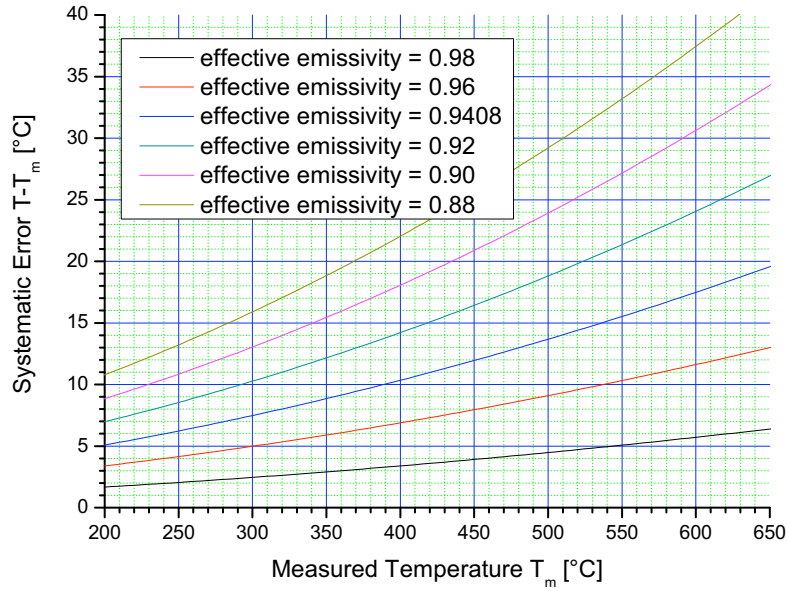
Figure 4.2: The error of the temperature measurement with a pyrometer versus the measured temperature values. The measurement error is plotted for different effective emissivities.

parameters for the calculation are listed in table 4.2.

$$\frac{1}{T_m} = \frac{1}{T} - \frac{\lambda}{c_2} \ln \epsilon_\lambda \qquad (4.1)$$

$$\Delta T = T - T_m = T - \frac{T}{1 - T\frac{\lambda}{c_2} \ln \epsilon_\lambda} = \frac{T_m}{1 + T_m\frac{\lambda}{c_2} \ln \epsilon_\lambda} - T_m \qquad (4.2)$$

T_m...	temperature measured by the pyrometer	c_2...	second radiation constant
λ...	operating wavelength of the pyrometer	ϵ...	effective emissivity
T...	temperature of the measured object	ΔT...	temperature difference

Table 4.2: Parameters for the calculation of the emissivity dependent measurement error.

c_2...	second radiation constant (taken from: [49] page 172)	$14.388\,\mathrm{mK\,m}$
λ...	operating wavelength of the pyrometer	$5.3\,\mathrm{\mu m}$
ϵ_{glass}...	emissivity of the substrate glass	0.97
T_{view}...	transmission of the view port [52]	0.97
ϵ...	effective emissivity (product of ϵ_{glass} and T_{view})	0.94
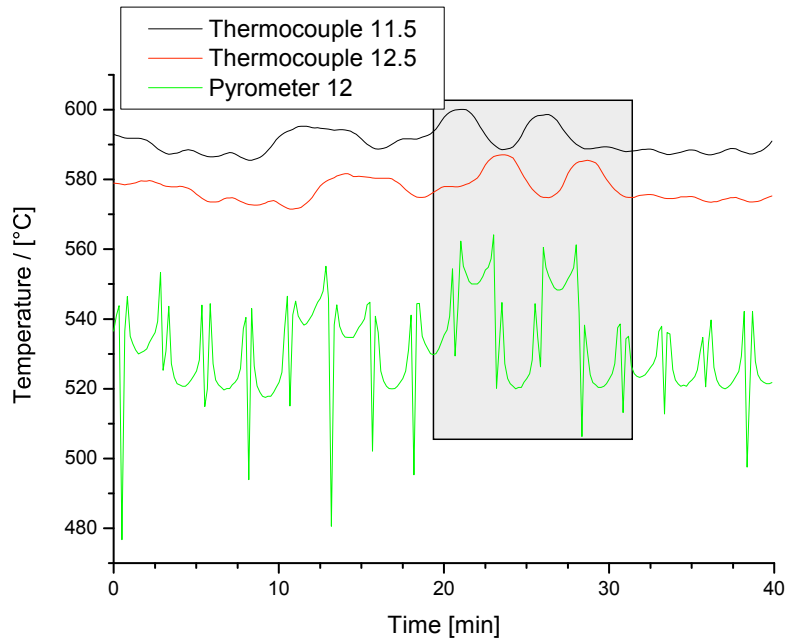
Figure 4.3: Temperature measurement during CIGS deposition at high temperature. The fresh substrates can easily be distinguished from the dummies.

4.3   Implementation in MP

To measure the temperature of any material with a thermocouple a good thermal contact is crucial. This applies for the thermocouple in the Se source which is dipped into liquid Se. Since the substrates in MP are moving, a direct thermal contact with the thermocouples is not possible. In contrary the thermocouples are not directly in touch with anything, hence the temperature of the thermocouples in a dynamic radiation balance is measured. In high vacuum heat transmission is performed only by thermal radiation which for a black body is described by Planck's law of blackbody radiation.

The materials surrounding our thermocouples are substantially different from black bodies and also have very different temperatures. If there was no temperature grading in the thermocouple's environment the thermocouple evidently finds its radiation balance at the same temperature. During deposition the radiation balance is mainly determined by the substrate heaters, the very close substrates and the cooled chamber wall in the back. To increase the sensitivity metal flags are mounted on the thermocouples which can be seen in figure 4.1 on page 35. The flags are mounted parallel to the backside of the substrates to maximize the substrates contribution of the substrates to the thermocouple's radiation balance.

4.4   Temperature measurements

The temperatures measured in MP are logged every ten seconds, enough to follow the substrates and to get a detailed picture of the temperature measuring process. In figure 4.3 on page 37 the temperature measured by pyrometer 12 and its two neighbouring thermocouples are shown in a standard deposition situation. The temperature signal from the pyrometer shows deep spikes every 2.5 min. These spikes result from the Mo substrate holders passing through the pyrometer's field of view. Like most metals, Mo is highly reflective and has a low emissivity within a broad range of wavelengths. The spikes allow us to deduce the exact position of the samples in the system. To investigate the influence of the substrate temperature we used two Mo coated SLG substrates for each deposition run. In figure 4.3 on page 37 the fresh substrates are easily identified, as they have higher temperature than the dummies. We 'spaced' the substrates leaving one dummy in between, to provide the most similar environment possible for both substrates. The lower temperature of the dummies results from the high integral emissivity of the thick CIGS layer formed after several depositions, as compared to the low emissivity of Mo. On the backside all dummies and substrates are fairly
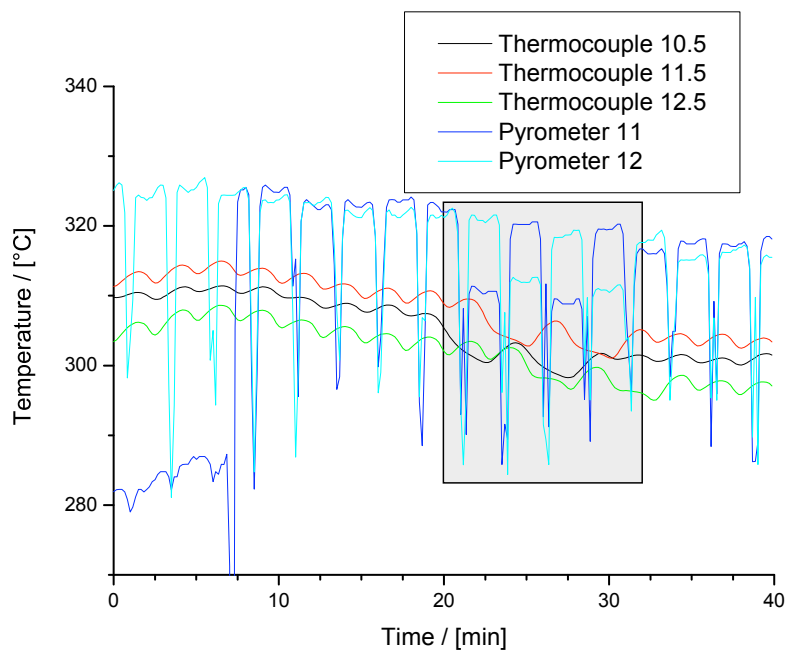
Figure 4.4: Temperature measurement during CIGS deposition at low temperature. The fresh substrates can easily be distinguished from the dummies.

identical and so is their ability to absorb radiation from the heaters. The undefined thickness of the CIGS layer on the dummies makes them individual, while substrates show a very similar temperature. Nevertheless after many runs the CIGS on the dummies seems to reach a thickness where small differences are not critical any more and these 'old' dummies behave quite similar to each other.

The shape of the signal from the pyrometer shows that reflected radiation from the lamps strongly influences the measurement, therefore the substrate temperature can be measured only in the middle between two spikes, where the pyrometer axis is normal to the substrate surface. The two pyrometers are outside the vacuum chamber looking through a view port on the substrates. The view ports are made of MgF_2 with a transmission of 97% at wavelength of $5.3\,\mu m$. To avoid Se condensation the view ports need to be heated and will therefore contribute to the measured radiation. As the view ports are highly transparent at the measured wavelength and only heated to about $150\,°C$ its influence can be omitted at least for measurements at high temperatures.

As all major sources of misleading contributions are strongly reduced or avoided or corrected the measured temperatures are very close to the absolute substrate temperature with an estimated error below $\pm10\,°C$.

4.5   Comparison of temperature sensors

The thermocouples are more individual in comparison to the pyrometers: they are not in identical positions with respect to the distance from the lamps or substrates, they might show a slight output shift due to ageing and their Mo absorption flags are coated with a material of unknown characteristics. Thermocouple 10.5 is a little different since it has a new flag that is still shiny, as can be seen on figure 4.1, and that might contribute to the relatively high measured temperatures with this device. Despite all difficulties the thermocouples show a reasonable and similar behaviour with less than $20\,°C$ divergence in a deposition at constant heating power. The signals of the thermocouples oscillate with the periodicity of the substrates, just as the spikes in the pyrometers signal. At least for the substrates the maxima of the thermocouple measurements coincide almost perfectly with the spikes of the pyrometer measurements. To make the measurements more comparable we used only the maxima at high temperatures. At low temperature we used the pyrometers spike to localize the right position for reading the temperature.

The offset in comparison with the pyrometers turned out to be temperature dependent. Figure 4.4 on page 39 shows the pyrometers and the closest thermocouples in a low temperature deposition. Here the substrates
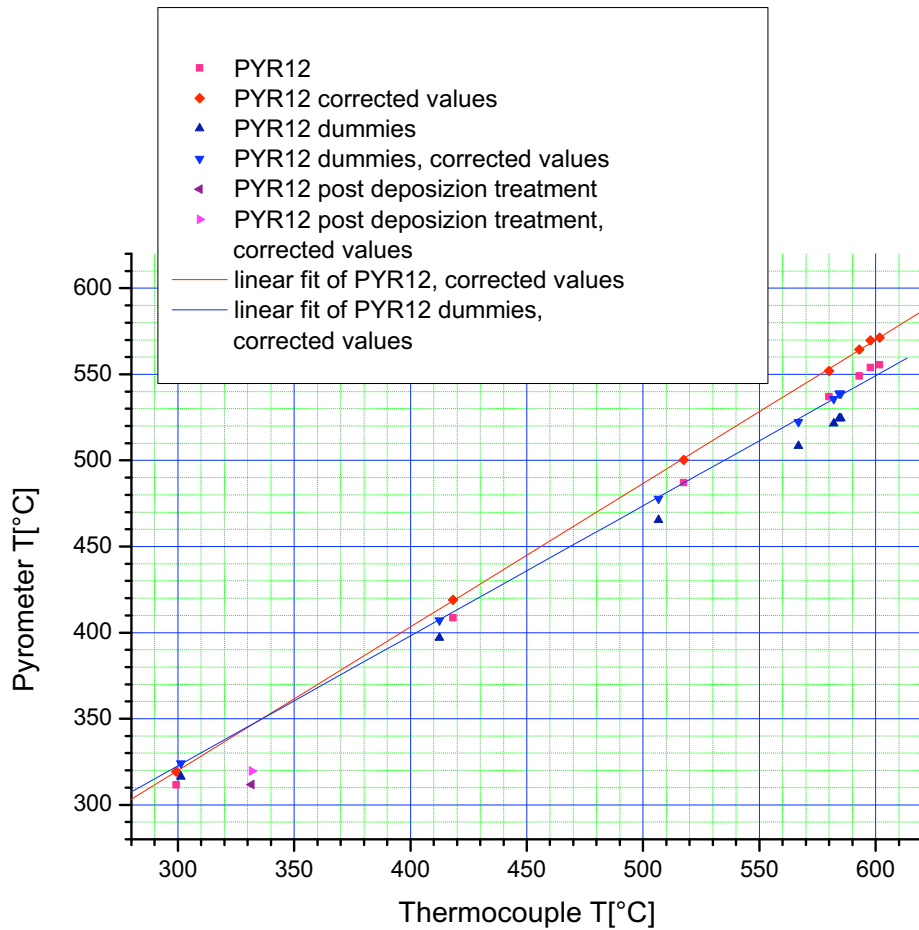
Figure 4.5: Plot of the temperature measurements with pyrometer 12 against the values of the neighbouring thermocouples. The measurements have been carried out during CIGS deposition at different temperatures. Additionally the values obtained in the post deposition treatment are plotted. The corrected values consider the effective emissivity of the substrates.

are colder than the dummies and the temperature measured by the pyrometers exceeds the thermocouple values. Figure 4.2 shows that the corrected value for the pyrometer is about 8 °C higher at 320 °C. The relation between the temperatures measured by the pyrometer and the neighbouring thermocouples is plotted in figure 4.5 on page 41. The values for this figure are obtained by calculating the arithmetic mean value of the temperature for two substrates measured at the thermocouples before and after the pyrometer. This value is plotted against the arithmetic mean value of the temperature measured at the 'enclosed' pyrometer. The values obtained at different deposition temperatures show a linear relation. As a help to find corresponding temperatures a linear fit was made.

In figure 4.5 on page 41 the comparison includes 'old' dummies and the post deposition treatment. The mean values are calculated for up to four dummies in a row which showed similar temperatures. Here the offset increases stronger with the temperature but a linear fit applies as well. The dummies are not as hot, as the substrates, their contribution to the radiation balance of the thermocouples is lower while the heater part remains the same. However when considering dummy temperatures one should keep in mind that they are individuals undergoing changes in every deposition. As described in the following section a post deposition treatment was performed with all substrates before further processing. For this step the substrates were heated up in MP without starting the sources. In this situation substrates are not heated by the sources but only from the substrate heaters which need higher power to reach equivalent substrate temperatures.

The corrected values from the pyrometer show deviations from the thermocouple measurements up to 30 °C. At high temperatures the thermocouples tend to show too high values, while at lower temperatures the deviation is the other way round. At about 420 °C the thermocouples values meet the pyrometer results. In the case of the dummies this point is reached at 430 °C. The dummies are a little colder at the same heating power since they emit more radiation on the coated side. This explains the relatively higher measurements with the thermocouples. The effect is stronger at higher temperatures. At 350 °C the lines cross, below this temperature the dummies are a little warmer.

In the case of the post deposition treatment the situation is different since the sources are turned off. The higher heater power results in higher values measured with the thermocouples. At 320 °C the thermocouples already show 10 °C more.

Chapter 5

Substrate temperature variation

5.1 Substrate heater power

The substrate temperature during deposition is usually constant at about 600 °C. More precisely the substrate heater power is constant for all heaters in the evaporation zone. The temperature is measured with the thermocouples on the backside of the substrates. As discussed above the real substrate temperature is somewhat lower. For simplicity, in this section only the temperatures measured with the thermocouples are discussed.

Three series of experiments have been carried out, the series will be herein after referred to as series A, B and C. Each series contains four CIGS deposition runs with different heating profiles. Two Mo-coated SLG substrates were coated in each run. The substrate heater power profile was changed in different ways during the three series. All series started with a constant heater power during deposition. In this standard procedure all heaters in the evaporation zone are set at 40 % of their maximum heating power, leading to the above mentioned constant substrate temperature of about 600 °C. This first run was performed in the same way in all series and can therefore be considered as a reference. For the following runs the heating power was reduced. In each of the series the heating was reduced in a unique way.

In figure 5.1 on page 44 the heater power for series A is plotted, showing a constant substrate heater power in the deposition zone. Starting at 40 %, the heating power was reduced by 10 % of the maximum heating power in the following runs. To realise a more constant temperature during deposition the substrates were overheated in the pre-deposition zone. These first six heaters were reduced in their power in the same way in series B and C. By this we ensure that the starting temperature for the substrates entering the deposition zone was the same for the corresponding runs in all series.
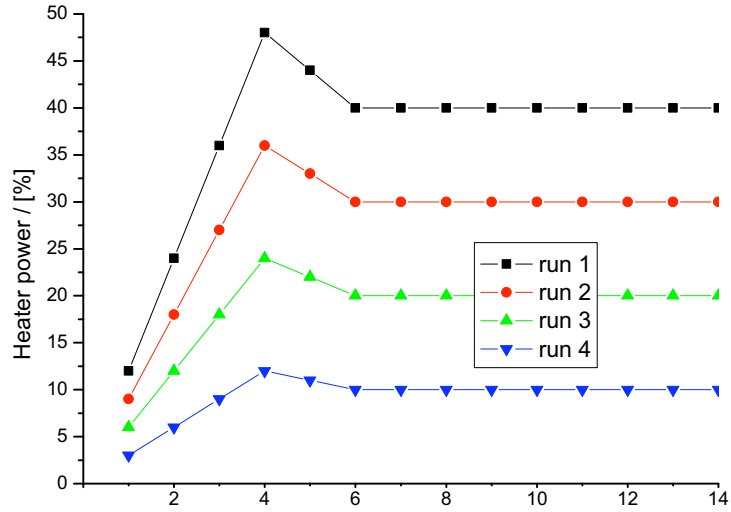
Figure 5.1: Heater power settings during CIGS deposition in series A
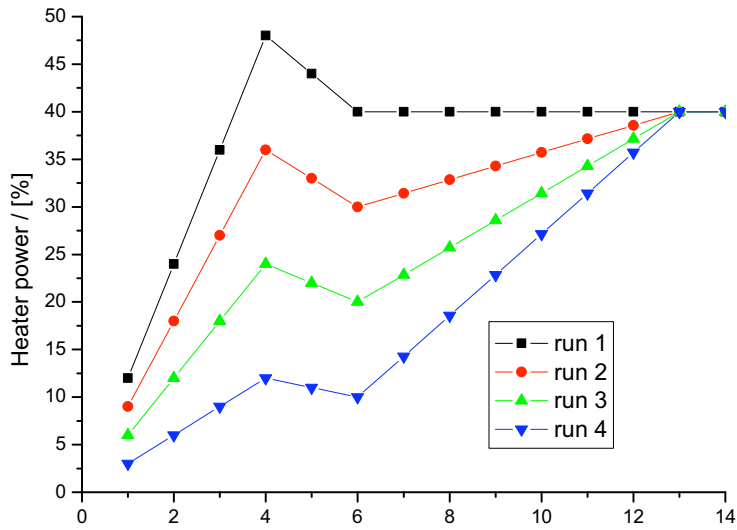
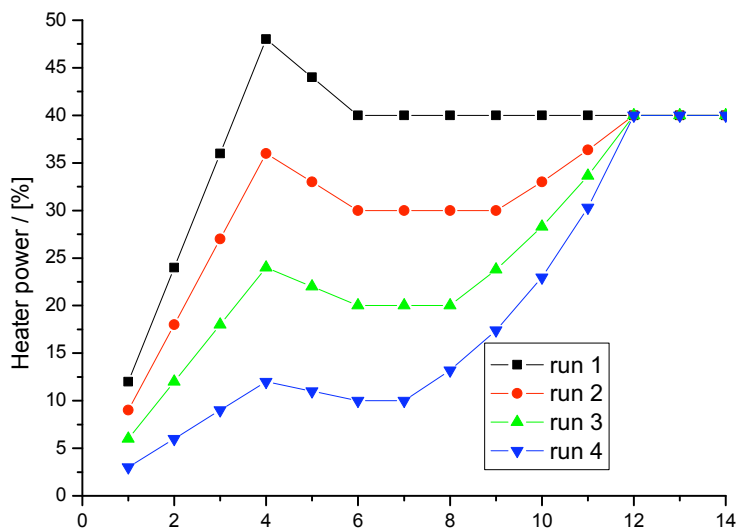Figure 5.2: Heater power settings during CIGS deposition in series B

Figure 5.3: Heater power settings during CIGS deposition in series C

Series B was performed with a constant increase of heating power during deposition. The last two heaters were held at 40 % for all four runs. Figure 5.2 on page 44 documents the steady increase of heater power in these series.

For series C the heater setting in the pre-deposition zone and of the last two heaters was the same as in series B. Whereas the increase of the heater power during deposition was not constant but roughly following an exponential growth. The resulting heater power is plotted in figure 5.3 on page 45. Compared to series B the heating increase is slower in the beginning of the evaporation zone while it rises faster towards the end.

5.2 Temperature profiles

The graphs in this section show the corresponding substrate temperatures during deposition for the above discussed heater power profiles. Except for the last run in series A, all temperature profiles at constant heating power show a decline of temperature towards the end of the deposition. The maximum temperature was measured at thermocouple 10.5. This is due to the increasing thermal emission of the CIGS film as it becomes thicker during deposition.

In figure 5.5 and 5.6 the temperature profiles of series B and C are shown. The temperature rises during deposition and the temperature maximum shifts to the end of the deposition zone.
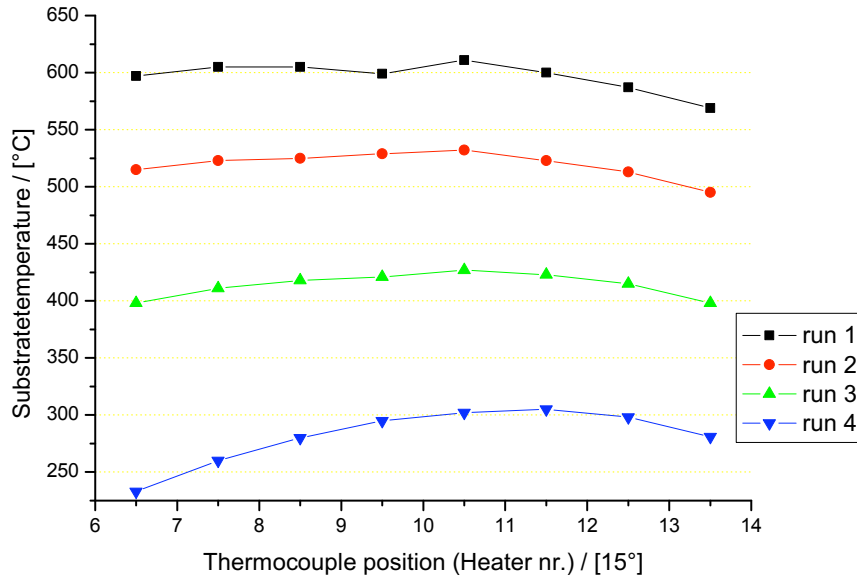
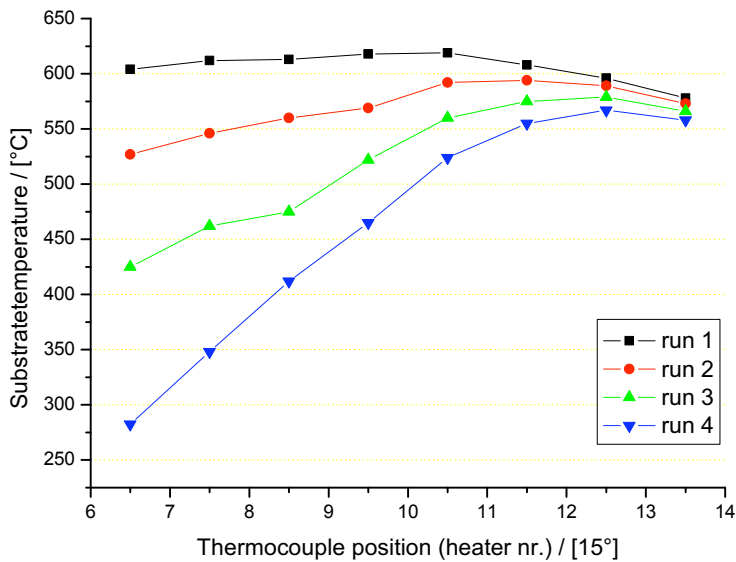Figure 5.4: Temperature profile during CIGS deposition in series A

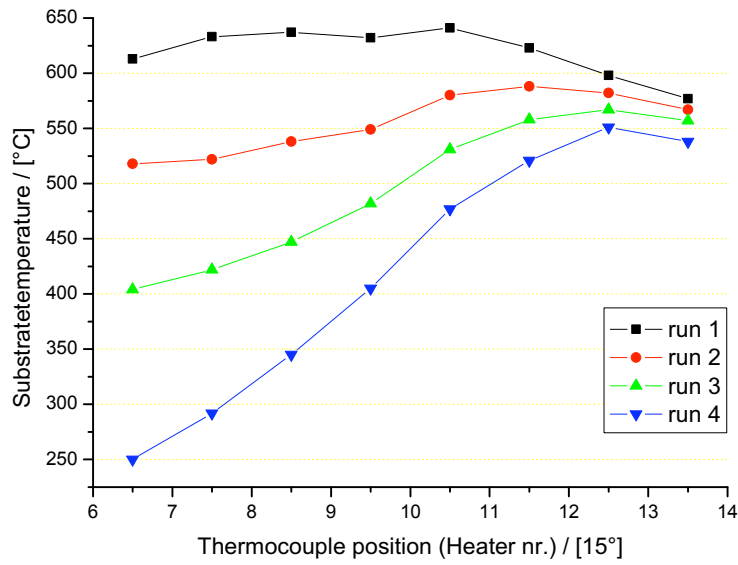Figure 5.5: Temperature profile during CIGS deposition in series B

Figure 5.6: Temperature profile during CIGS deposition in series C

In series C the first run shows a higher temperature reaching a maximum at about 650 °C. This results from a non linearity in the power control of the heaters. The deviation from a linear behaviour was measured and explained only after the experiments were performed.

Chapter 6

Measurements and Results

From the CIGS deposition we obtained two $12.5\,\mathrm{cm} \times 12.5\,\mathrm{cm}$ SLG-MO-CIGS substrates in each run. One of the substrates was in the next step covered with Zn(O,S) in the ALD reactor. From the other substrate a central $5\,\mathrm{cm} \times 5\,\mathrm{cm}$ 'fillet' piece was cut out. The fillet was covered with CdS in the chemical bath deposition. Further processing was identical for both buffer layer types following the baseline process described in chapter 3. After scribing we cut four $5\,\mathrm{cm} \times 5\,\mathrm{cm}$ from the Zn(O,S) substrates to ease handling in the following measurements: IV (current-Voltage) characterisation in light, external quantum efficiency and some cells were finally cleaved to look at cross-sections in the SEM (Scanning Electron Microscope).

The remaining parts of the substrate of which we cut out the fillet for the CdS cells were used for analysis of the CIGS layer. We performed XRF composition and thickness measurements, XRD Se-detection on the surface and Profilometer thickness measurements.

6.1 Composition and thickness of the evaporated CIGS layer

To analyse the composition of the CIGS layer we cut a piece of the substrate after the deposition in MP. A Spectro X-lab 2000 XRF-system (X-ray fluorescence) serves to measure the elemental composition of the layer. Calibration of the system is performed by measuring a reference sample of known composition first. In order to make the results as comparable as possible all samples have been measured on the same day one after the other. From each substrate the piece on the left and on the right side of the 'fillet' has been analysed. In the figures the arithmetic means of the two values are plotted. The two pieces from the left and the right were compared to control the
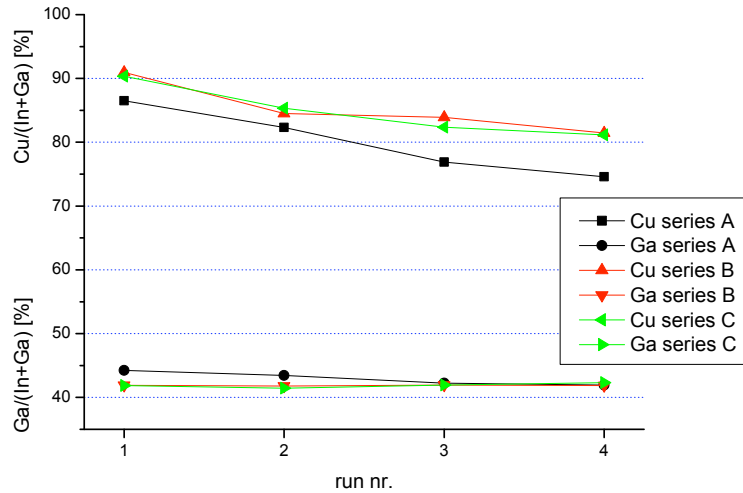
Figure 6.1: Composition of the CIGS layers deposited at different substrate heating profiles

homogeneity of the CIGS layer. The maximum observed difference between the left sample and the right one was 2.7 percent of the composition.

The composition of the samples is calculated by comparing the XRF counts of each sample to the XRF counts of the reference sample using a linear model. The linear model is reasonable as the reference is similar to the measured samples. Se was evaporated in excess, and the XRF results do not indicate substantial amounts of Se vacancies.

Composition results are shown in figure 6.1. The graphs are labelled as series in the legend in accordance to the heater and temperature profiles described in chapter 5. The numbers scaling the X-axis refer to the four runs of each series. The drawn lines between the individual runs are only guides to the eye, indicating run-to-run trends.

The graphs show the relative Cu content decreasing with the heater power in all series. The Ga to In ratio is almost constant at about 42 percent of Ga. Only in series A, in which the heater power is (equally) lowered in the whole deposition region, the Ga content is decreasing slightly with the substrate heating power.

The sum of the XRF counts for Cu, In and Ga provides the base to calculate the thickness of the CIGS layer in comparison to the reference. This is the standard procedure to estimate the thickness of the layer. Additionally we measured the thickness with a Dektak V200-Si Profilometer. To gauge the
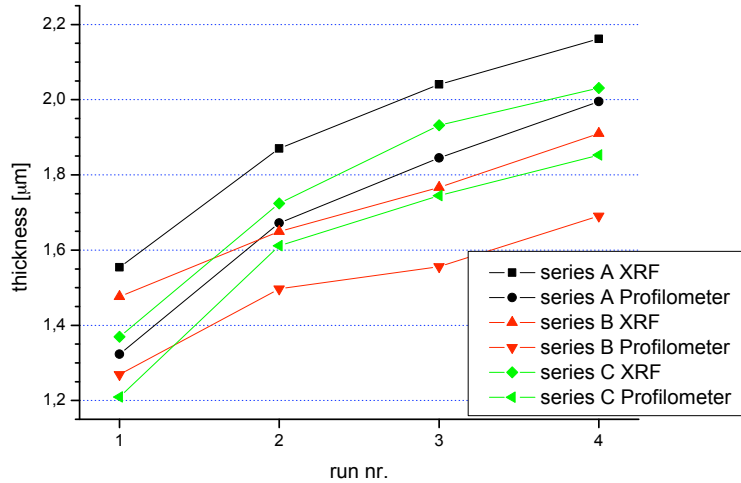
Figure 6.2: Thickness of the CIGS layers deposited at different substrate heating profiles

Profilometer a 955.4 nm calibration step was used. We scratched off the CIGS from the Mo with a needle and measured the step height. We measured the sample on the left of the fillet. On each piece eight steps have been analysed. The largest value for the sample standard variation was below 20 nm. In figure 6.2 the arithmetic mean values of the profilometer and the values from XRF analysis are plotted.

Beside a offset the two thickness measurements coincide very well. The overestimated thickness of the XRF measurements may be caused by unavoidable scratches after heavy use on the XRF reference sample. This shows that the reference sample is a little worn out. Therefore absolute thickness calculated from XRF data is not fully reliable, but trends within one series of measurements are not affected. The composition measurements do not seriously suffer from the worn out reference sample since all components are equally reduced by scratches.

The results show that the thickness grows up to 50 percent when the substrate heater power is reduced. This increase in thickness takes place in a similar way in all three series.
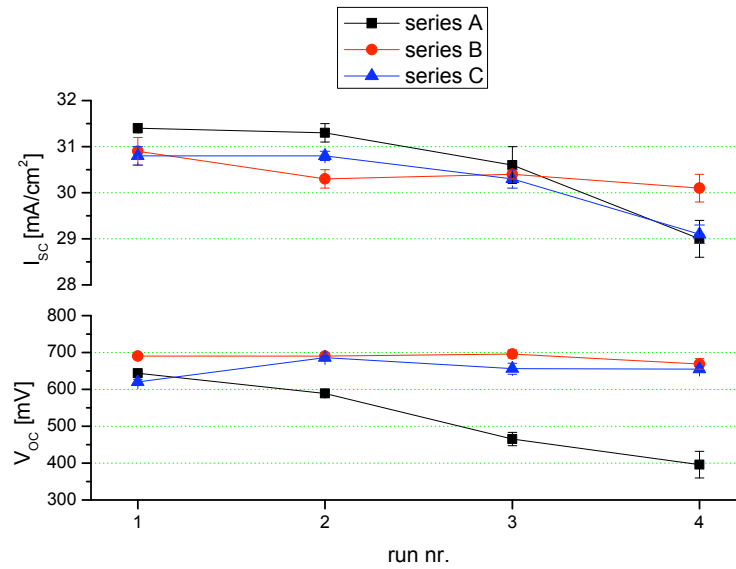
Figure 6.3: Average Isc and Voc of the cells fabricated with the CIGS layers deposited at different substrate heating profiles
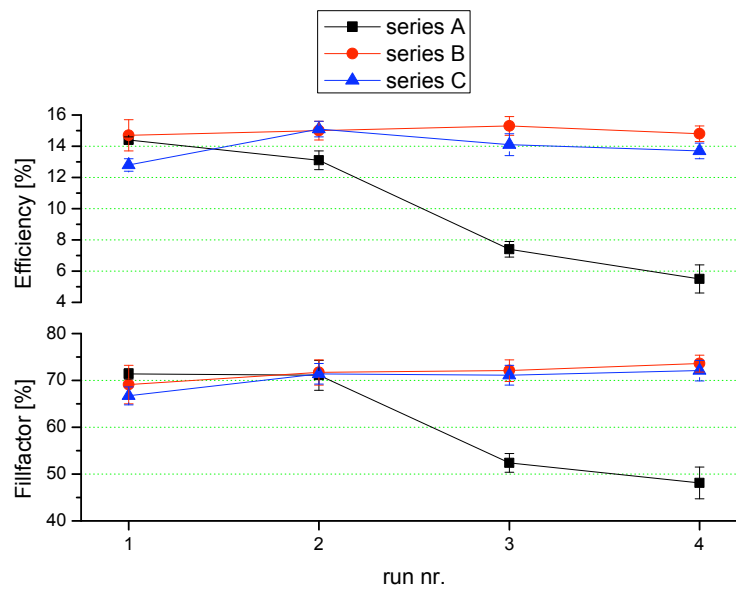

Figure 6.4: Average efficiency and fill factor of the cells fabricated with the CIGS layers deposited at different substrate heating profiles
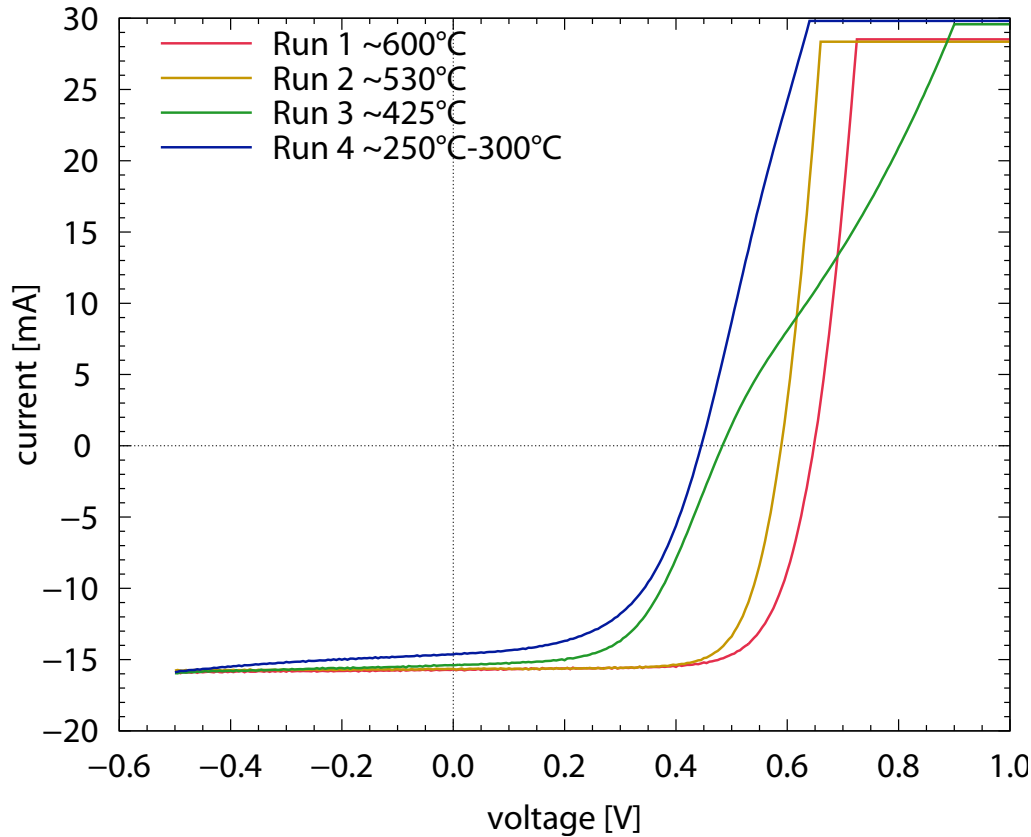
Figure 6.5: Current Voltage characteristic of selected cells from the four deposition runs in series A

6.2 IV Measurement

An ELH projection halogen lamp provides the light for the IV measurement. The distance between the lamp and the solar cell can be adjusted in order to ensure a light intensity of $1000\,\mathrm{W/m^2}$ at the cell surface. A silicon reference solar cell is used for calibration. Since the lamp changes its intensity during its lifetime, a recalibration is done every 20 min to provide constant conditions for all measurements.

The cells with a $Zn(O, S)$ buffer layer showed very low and unstable open circuit voltage in all samples. The reason for their weak performance might be due to a malfunction in the ALD deposition or maybe a change in the CIGS surface during the post deposition heating. Since the The $Zn(O, S)$ cells could neither match with the results from previous experiments nor with those from the CdS cells we decided to neglect these results in the context of this project. In the following only the results of the CdS cells are
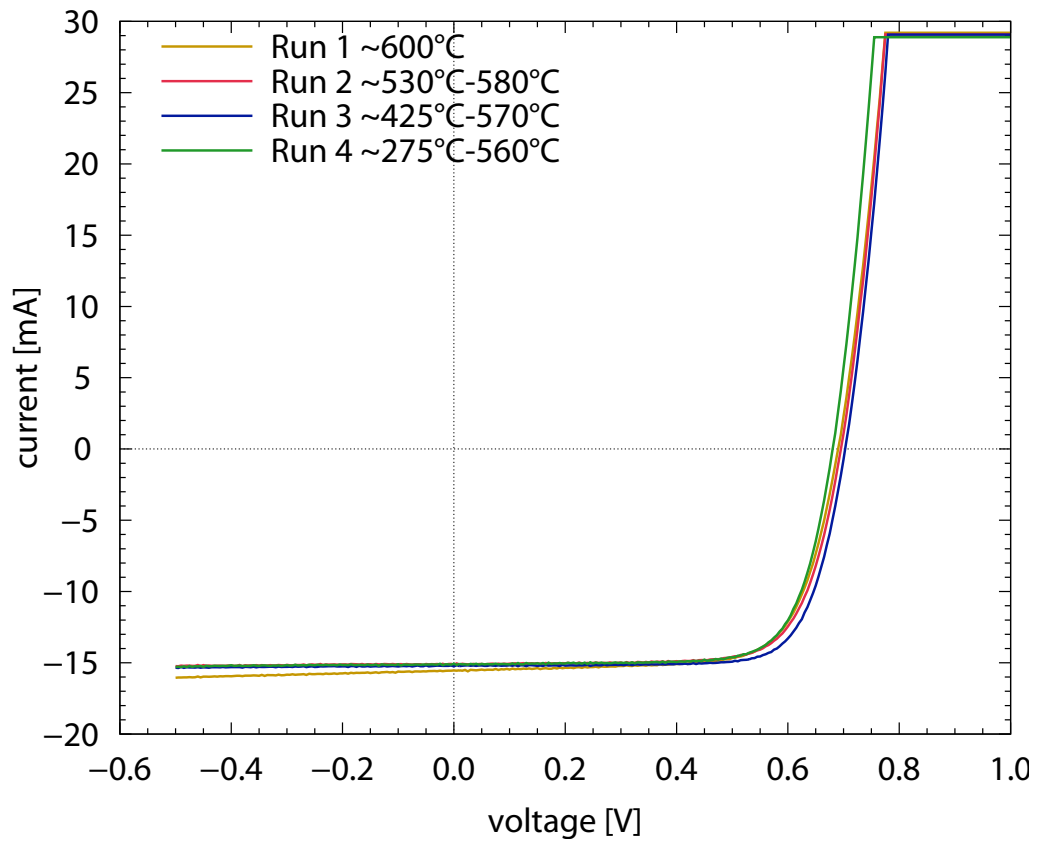
Figure 6.6: Current Voltage characteristic of selected cells from the four deposition runs in series B
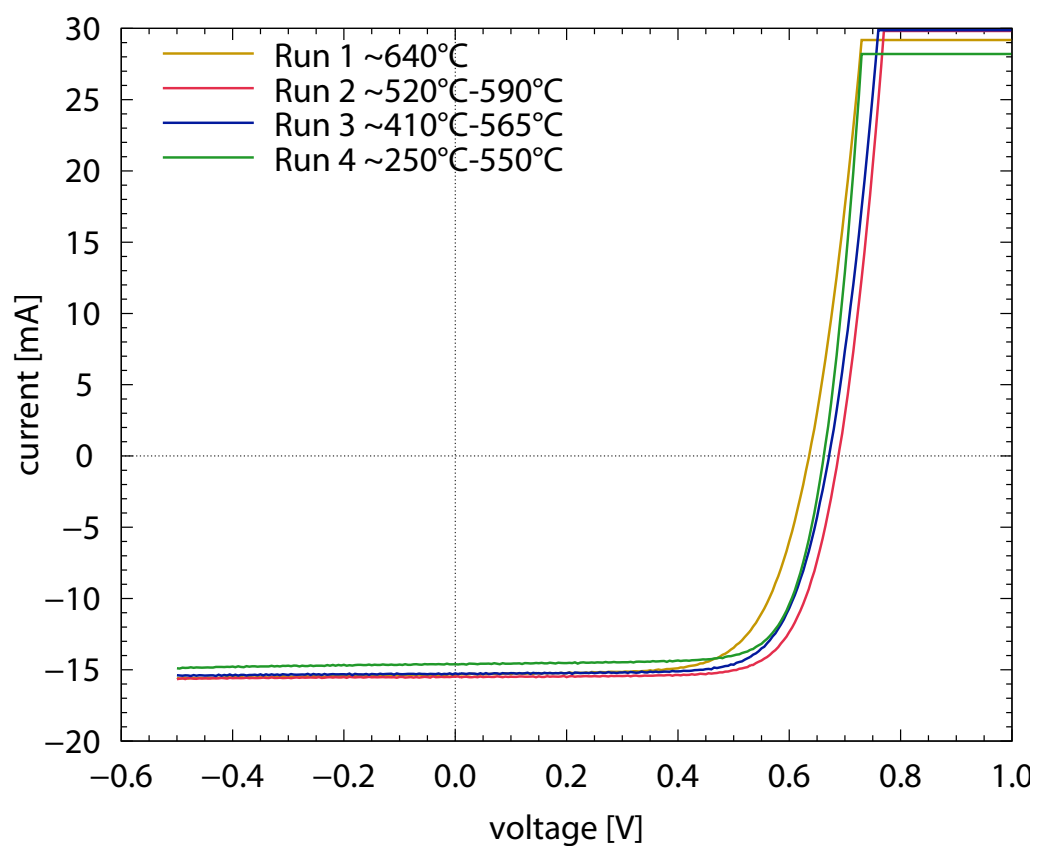
Figure 6.7: Current Voltage characteristic of selected cells from the four deposition runs in series C

shown and discussed.

On each of the $5\,\text{cm} \times 5\,\text{cm}$ samples four columns of eight $10\,\text{mm} \times 5\,\text{mm}$ solar cells have been defined in the scribing process. IV-measurements of the first two columns have been carried out. The results from the sixteen analysed cells of each sample form the basis for a statistical evaluation. The arithmetic mean values and the standard deviation, calculated from equations 6.1 and 6.2 are plotted in figures 6.3 and 6.4. To identify outliers the concept of quartiles in descriptive statistics was applied. The calculation of the upper limit for outliers follows equation 6.3, results below the limit have not been considered calculating the mean values and deviations.

$$\bar{x} = \frac{1}{n} \sum_{i=1}^{n} x_i \tag{6.1}$$

$$s = \left[\frac{1}{n-1} \sum_{i=1}^{n} (x_i - \bar{x})^2 \right]^{\frac{1}{2}} \tag{6.2}$$

$$ULO = Q2 - 1.5(Q3 - Q1) = Q2 - 1.5 IQR \tag{6.3}$$

$s...$	spectral radiance	$n...$	frequency
$x_i...$	absolute Temperature	$\bar{x}...$	Planck constant
$ULO...$	Upper Limit for Outliers	$Q1...$	lower quartile
$Q2...$	median	$Q3...$	upper quartile
$IQR...$	Inter Quartile Range		

Both V_{oc} and fill factor decline strongly at low substrate temperatures in series A. These properties lead to low conversion efficiency of CIGS solar cells coevaporated on 'cold' substrates. Several investigations on substrate temperature during CIGS coevaporation with similar outcome have been published [42, 43, 44, 45, 53]. In all series the current shows a minor decline at reduced substrate heating. Unlike series A, in series B and C the V_{oc} is almost constant while the heating is reduced. The fill factor even tends to show a slight increase at reduced heater power in series B and C.

In the figures 6.5 to 6.7 the current voltage characteristic of a selected cell of each run is plotted. In series A the decline of the cell performance from run one to four is obvious. In series B and C the curves are very similar.
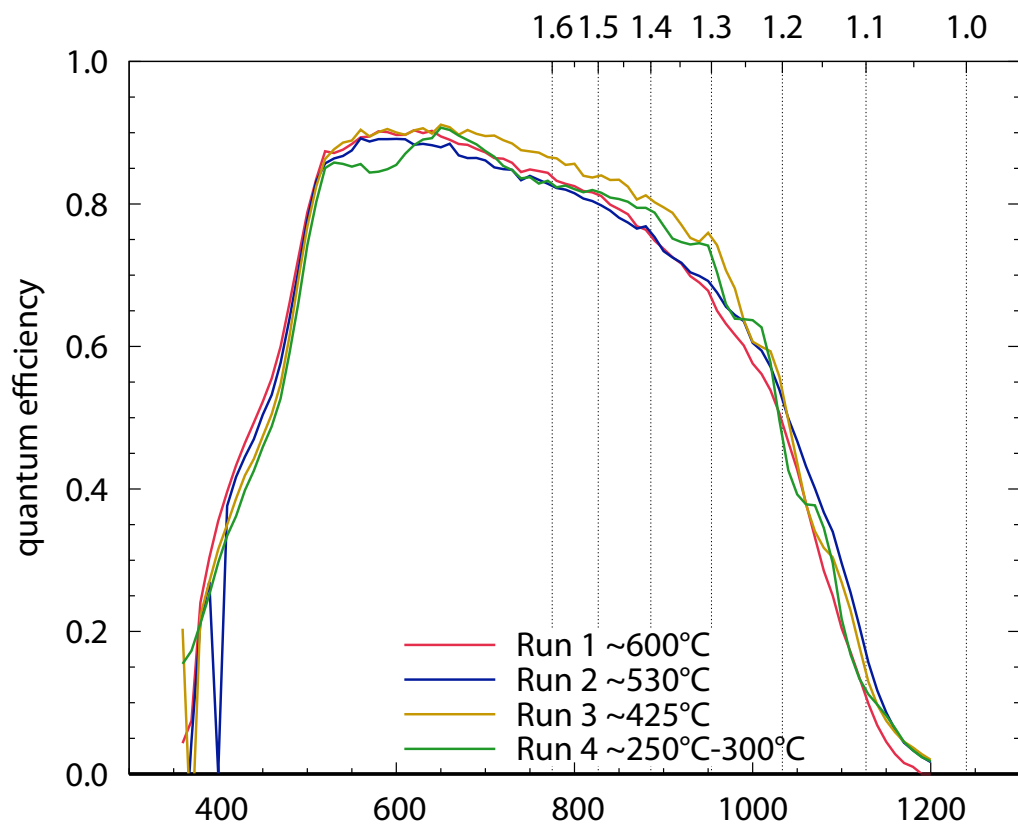
Figure 6.8: External quantum efficiency of selected cells from the four deposition runs in series A
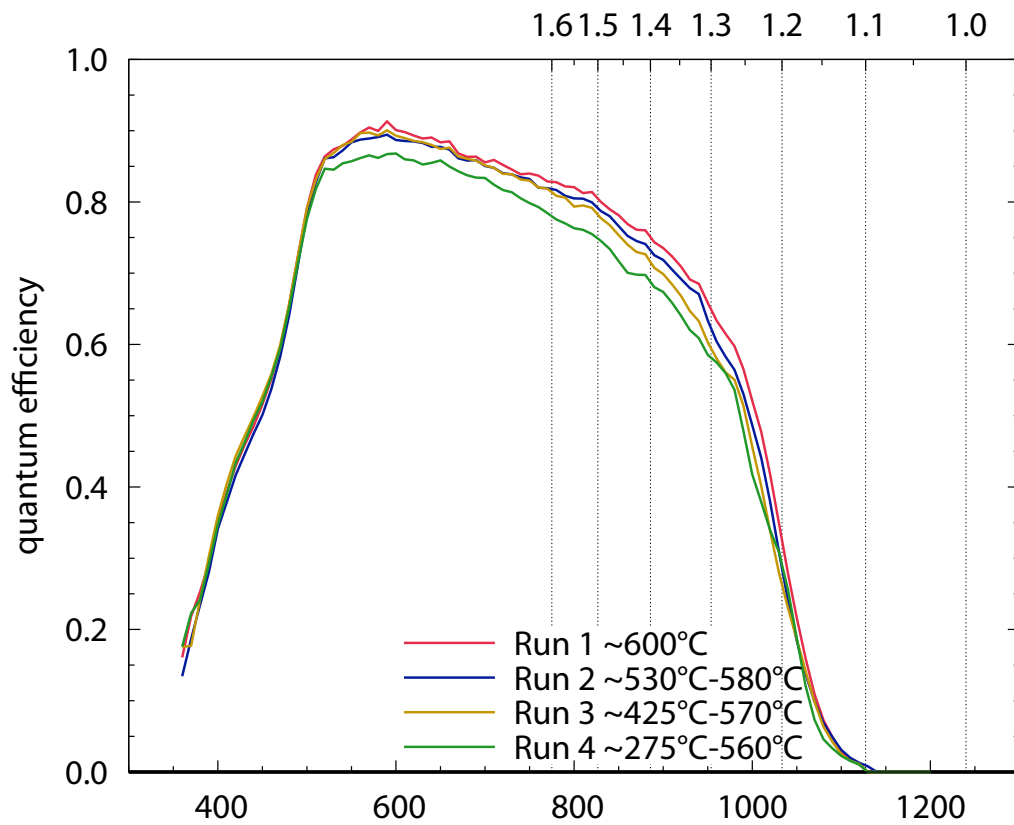
Figure 6.9: External quantum efficiency of selected cells from the four deposition runs in series B
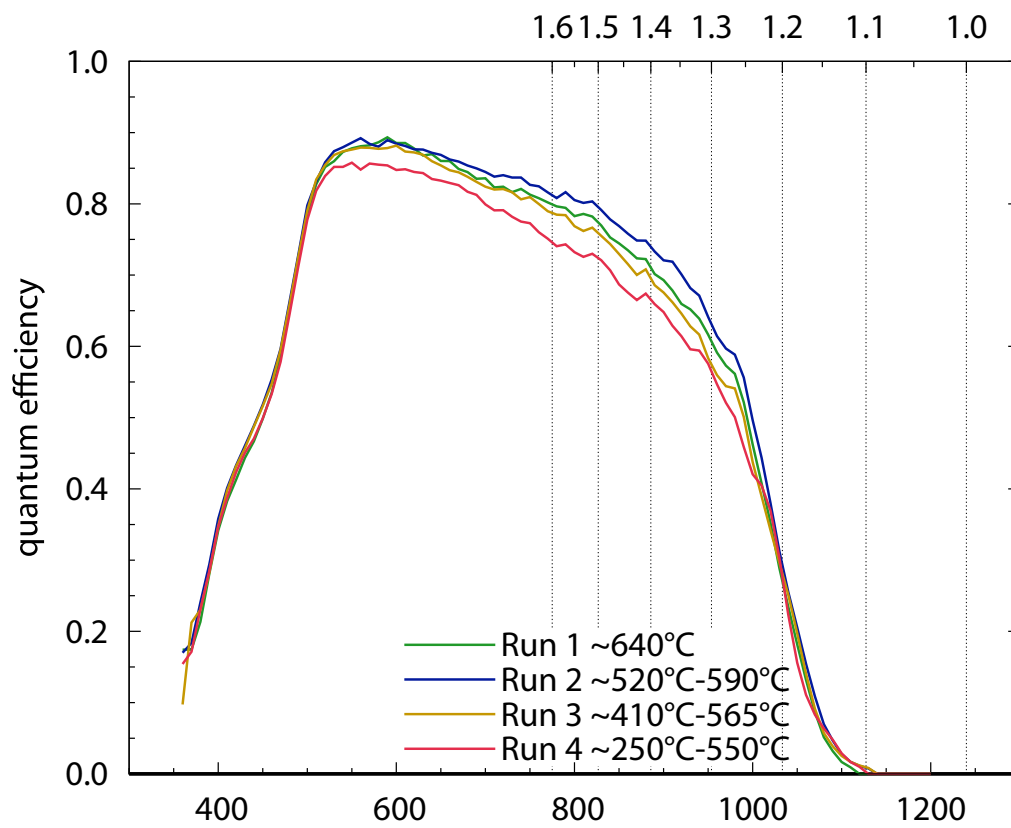
Figure 6.10: External quantum efficiency of selected cells from the four deposition runs in series C

6.3   EQE

EQE (External Quantum Efficiency) shows the conversion efficiency in dependence on the photon energy (wavelength). In our setup a xenon arc lamp provides the light, diffraction gratings work as monochromators, additional filters remove the harmonic content. A fibre optical waveguide leads the light of the desired wavelength to the analysed cell. The wavelength range from 350 nm to 950 nm is calibrated with a silicon diode and the range from 950 nm to 1300 nm with a Ge-cell.

In accordance with the results from the current voltage characteristics the EQE results are very similar for all cells in all series. In series A the absorption extends to longer wavelengths as compared to series B and C. This indicates that the minimal bandgap in the CIGS layer is slightly lower in series A. Quantum efficiency drops sharply at about 510 nm because here the CdS buffer layer with its bandgap of 2.42 eV starts to absorb.

The EQE of series A run 4 exhibits a kink at 620 nm, probably due to a small amount of crystalline Se on the CIGS layer. In series B and C run 4 shows a little lower EQE as compared to the other runs.

6.4   Scanning Electron Microscope

To get a picture of the crystals in the CIGS layer we used SEM-SE (Scanning Electron Microscope with a Secondary Electron Detector). The type was a LEO 1550, with an in-lens detector. The working distance was at 3 mm to 5 mm and the magnification 5×10^4 and 10×10^4.

We cleaved samples with finished cells. The resulting piece was put in the microscopes sample holder and the fresh fracture surface was analysed.

The pictures show two to three main layers. On top the raspberry like structure is the transparent Al:ZnO front contact. The comparatively thick layer below the front contact is the CIGS absorber. The CIGS structure changes with the temperature profiles. On some pictures in the bottom a layer that looks like a stack of fine needles appears, which is the Mo back contact. At a close look, between the CIGS and the front contact the CdS buffer layer can be identified in a few cases. The pictures resolutions offer the possibility to zoom into details.

Figure 6.11 gives an overview of the CIGS layers deposited at different substrate temperatures. Crystal size decreases clearly at lower substrate temperatures. The very large crystals in the top picture result from a deposition at about 630 °C in the first run of series A. The temperature in this run was the highest in the project. The substrates were bend and the crystals nice
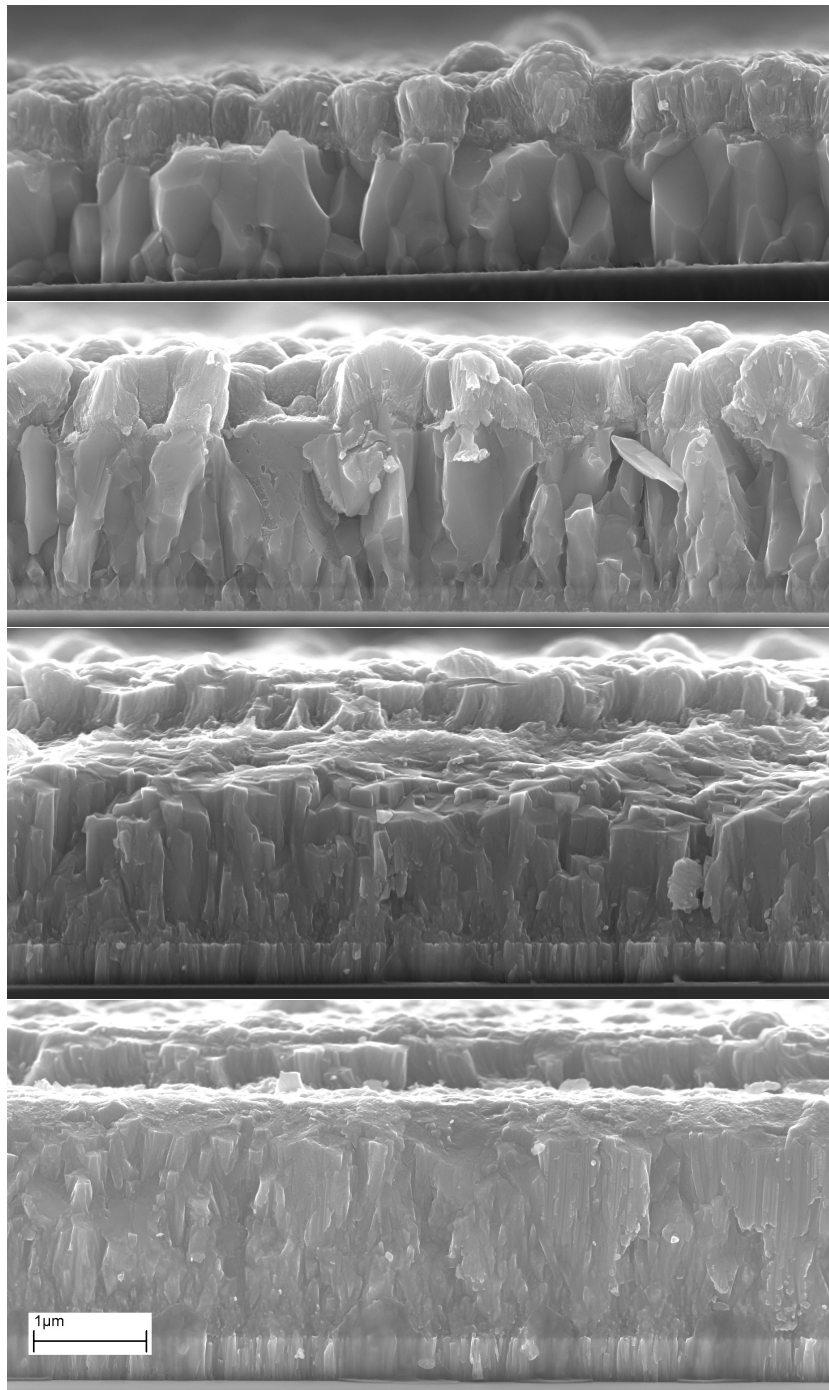
Figure 6.11: CIGS deposited at different substrate temperature profiles
From top to bottom: Series C run 1 (∼640 °C); Series A run 2 (∼530 °C),
run 3 (∼425 °C) and run 4 (∼250 °C to 300 °C)
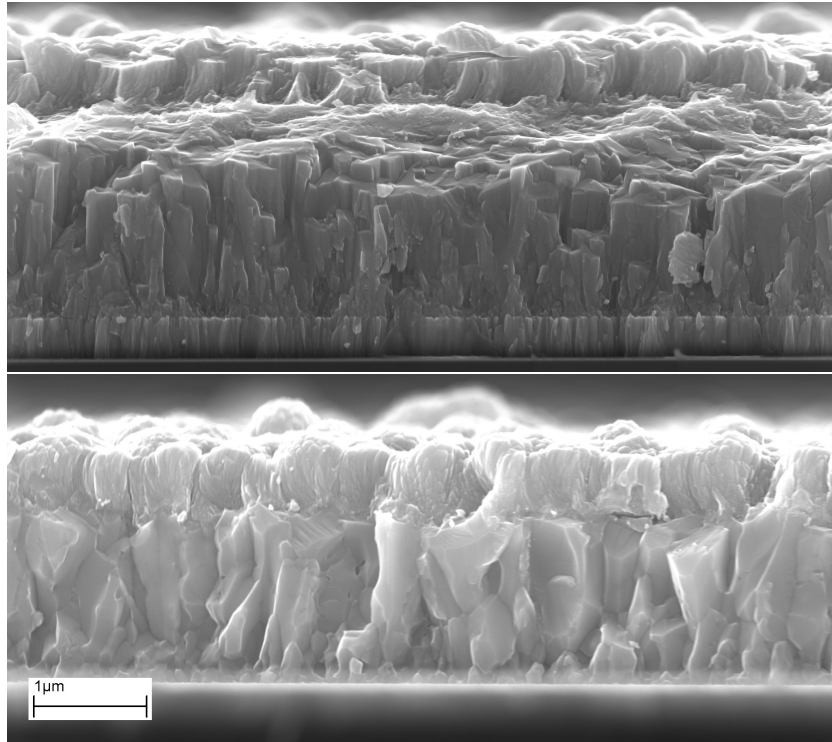
Figure 6.12: CIGS deposited at different substrate temperature profiles
Top: Series A run 3 (∼425 °C); Bottom: Series B run 3 (∼425 °C to 570 °C)
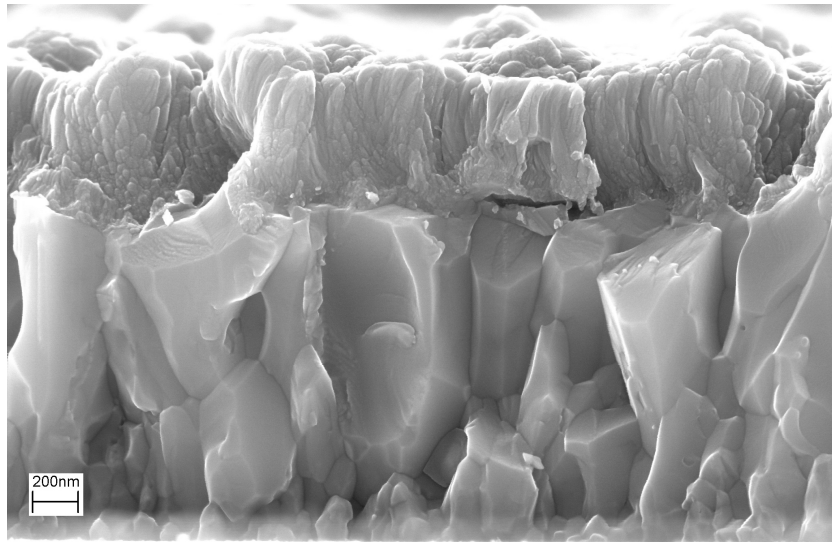
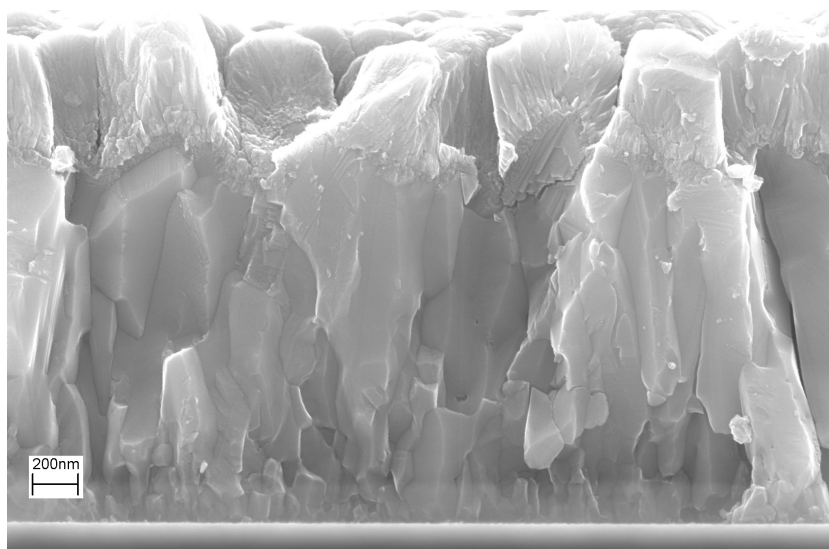

Figure 6.13: CIGS deposited in Series B run 3 (∼425 °C to 570 °C)

Figure 6.14: CIGS deposited in Series A run 2 ($\sim$530 °C)

and big, but the cell performance was weak compared to the runs at slightly lower temperature. The following pictures are taken from cells of series A deposited at about 520 °C, 410 °C and 290 °C. The corresponding temperature profiles are shown in figure 5.4. All temperatures are measured with the thermocouples, but can be 'translated' to absolute temperature values with the help of figure 4.5. At the two samples deposited at lower temperature the Mo back contact (needles in the bottom) and the CIGS broke in one plane while the top Al:ZnO layer shows a little setback. The other two samples show one plain for Al:ZnO and CIGS, but here the Mo layer broke too far away to be in focus together with the CIGS. This behaviour reflects different adhesive properties at the CIGS/Mo interface. All samples show smaller crystals near the Mo layer where the crystallization starts. While in the very hot run only a few small crystals remain, the cold runs show the influence of the Mo structure in the nucleation regime.

A comparison of two samples which entered the deposition zone at almost the same substrate temperature is given in figure 6.12. Both depositions started at about 410 °C but while the substrate temperature remains low in the upper sample's deposition (series A run 2), it rose up to 570 °C in the lower sample's deposition (series B run 3).

Finally we tried to find the maximum reasonable magnification. The pictures in figure 6.13 and 6.14 show what we achieved. In the second image the CdS layer can be found easily. Both pictures offer a detailed view in the

cells inner structure.

Chapter 7

Discussion and Conclusions

Three series of experiments have been carried out to study the influence of the substrate temperature on CIGS formation. From the results presented above some questions arose. Here I will try to explain the possible reasons for the observations and consequences for future experiments. Studying of literature and intense discussions with my colleagues at the Angström Solar Center were essential for the development of interpretations of the results.

7.1   Expected results

The three series of experiments are named series A,B and C in chapter 5. In series A deposition runs at constant substrate temperatures have been analysed. In four runs CIGS was deposited at different substrate temperatures. This series with depositions at constant substrate temperature is similar to experiments performed by various other researchers. So are the results presented in chapter 6 which served as a baseline. The influence of low substrate temperature on CIGS formation is discussed in chapter 2.

The structure of the material is strongly affected by the substrate temperature. At lower temperatures the crystals are much smaller. The photovoltaic performance is very weak due to low V_{oc} and fill factor. Several investigations show that the poor performance is mainly a result of insufficient Na indiffusion from the SLG substrate into the CIGS layer. Low substrate temperatures also result in low crystal quality. In combination with reduced Na indiffusion this leads to very poor photovoltaic performance.

7.2   Thickness, composition and selenium

The composition of the CIGS layer turned out to be quite stable.   The Ga/(In+Ga) ratio did not change at all in series B and C. In series A only a small decrease of the ratio is observable at lower temperatures, see section 6.1.

The relative Cu content of the CIGS layer decreases at lower substrate temperatures. This was observed in all series of experiments, the effect is slightly stronger in series A. As will be discussed in the following, this decrease in relative Cu content is accompanied by an increase in thickness and is probably caused by reduced scattering of indium and gallium in relation to copper.   Earlier experience and results during the preparation for this work showed that the Cu content is not critical in a broad range from about 70 percent up to 95 percent.

The thickness of the CIGS layer appeared to increase strongly at lower substrate temperatures. This seems to be natural at first sight. In general at lower temperatures the adsorption increases and the desorption decreases. Additionally nucleation is much faster at low temperatures. However both effects can not explain the huge increase in thickness of about 50 percent and more. Nucleation is a a very fast process even at the high deposition rates we used. Desorption is not critical even at 600 °C in accordance with the high melting point of the CIGS material. Compare chapter 2.2.3 and [40].

The main reason for the great increase in thickness at lower temperatures must be a growing number of particles reaching the substrate. The sources in MP are very stable and precisely controlled. The temperature log showed stable source temperatures in all series of experiments. Therefore the increase in thickness can not be caused by a greater flux from the sources.

The only remaining reason for the observed results is scattering in the Se cloud in front of the substrates. At first the explanation seems strange since we use an ultra high vacuum system to avoid any scattering in the deposition process. Indeed we had excellent base pressure of about 3×10^{-5} Pa. The pressure measurements during deposition did not show critical values at any time. The standard pressure gauge showed values of about 10^{-3} Pa during runs at high substrate temperature. The pressure dropped in all series of experiments as we lowered the heater power. In the last deposition run the pressure was at about 10^{-4} Pa. Both gauges showed similar pressure values. However one has to keep in mind that the gauges are more or less protected from the Se in order to avoid corrosion.

The mean free path can be calculated if the collision radii of the involved particles are known. Equation 7.1 and equation 7.2 are taken from [54] page 37 and 39.

$$\Lambda = \frac{1}{\pi\sqrt{2}(r_1 + r_2)^2 n} = \frac{kT}{\pi\sqrt{2}(r_1 + r_2)^2 p} \qquad (7.1)$$

$$\Lambda_{a293} = 0.665cm \cdot \frac{1}{p[Pa]} \qquad (7.2)$$

Λ...	mean free path	r_1, r_2...	collision radii of the particles
k...	Boltzman constant	T...	temperature
p...	pressure	Λ_{a293}...	mean free path of air at $293\,\mathrm{K}$
n...	number density	$p[Pa]$...	pressure in Pascal

The mean free path depends on the pressure and the collision radii of the involved particles. The mean free path of air can serve as a guideline. Se evaporates in rings of eight atoms or chains of individual length. Thus the collision radius will not be smaller than the collision radius of air. Table 7.1 shows the mean free path for several gases at 20°C.

Table 7.1: Mean free path, Λ, of selected gases at $20\,°\mathrm{C}$. The values are deduced from a diagram in [55] page 432.

Gas	C_2H_5OH	H_2O, CO_2	He
pressure [Pa]	Λ [cm]	Λ [cm]	Λ [cm]
1	0.2	0.4	2
0.1	2	4	20
0.01	20	40	200
0.001	200	400	2000

We have not directly measured any pressure that would predict scattering. But taking into account that the pressure gauges are not directly mounted in the deposition region it seems very reasonable to suggest Se scattering as the reason for thin CIGS layers at high temperatures.

In the following I will describe the situation in MP and present some arguments that support the theory of Se scattering.

As mentioned in chapter 2 Se is always evaporated in excess in the CIGS co-evaporation process. In MP the Se source is a simple pot protected with a cap that allows evaporated Se to escape. As indicated in figure 3.4 the

Se source is located near the heaters in the warm up zone. Se does not condensate on hot surfaces, unless it is incorporated in a compound like CIGS or Cu_xSe. Only the relatively cold parts in the system serve as a Se trap. This explains the higher Se pressure when the system is heated up. The heaters 4, 5 and 6 in the warm up zone received the highest power, as can be seen in the figures 5.1 to 5.3 . The strong heating near the Se source in the high temperature runs certainly supports the Se in reaching the evaporation zone. In all series of experiments we observed falling pressure at reduced substrate heater power. The Se pressure can be considerably higher in the very hot regions of the system. The relatively cold walls close to the pressure gauges serve as Se traps. It is difficult to quantify the underestimation of the measured Se pressure, but the obvious scattering of metals is a clear indicator of a dense Se cloud in front of the substrates.

In series B and C a part of the system is kept at high temperature in all runs. In the critical region near the Se source the temperature is reduced in the same way as in series A . This explains the similar increase of thickness at reduced heater power. The hot regions at the end of the deposition zone are of only little influence on the Se cloud near the substrates.

In series C the first run was a little more heated as compared to all other runs. The thickness in this run is the lowest of all depositions made for this work.

Sufficient Se is very important for the growth of high quality CIGS layers. Surface Se should be avoided but at the same time Se vacancies in the surface are a known reason for poor performance.

In general Se is simply evaporated in excess. Our experiments show that the CIGS formation is very stable at high Se pressure. Nevertheless for a reasonable use of raw materials Se evaporation should be significantly reduced. Several groups presented concepts for a more effective use of Se. Cracking of the large Se molecules could make the material more reactive and might open a way for improved CIGS formation [21, 22, 23, 24]. In our case the deposition can probably be much faster with less Se in the system.

7.3 Photovoltaic device performance

High photovoltaic performance of the CIGS layer is the central goal of all efforts. The substrate temperature during deposition is a key parameter for high quality CIGS layers. The results in this work show that lower temperatures at the start of the deposition have only minor influence on the materials performance. The results presented in chapter 6 demonstrate that very high efficient CIGS can be produced if the deposition starts at temperatures as

low as 300°C. Both IV curves and EQE measurements show the strong performance of the CIGS produced in series B and C. Small losses in I_{sc} are almost completely compensated by improved fill factors.

Starting the deposition at low temperatures does not diminish the device quality if high substrate temperatures of about 600°C are reached towards the end of the deposition. This result is almost ideal since the substrate temperature in a high throughput in-line system is expected to rise similar to our experiments.

A closer look to the results in the figures 6.4 and 6.3 in combination with the temperature profiles from chapter 5 gives rise to the following interpretation.

- A reduction of the substrate temperature from 590°C to 520°C leads to a small but significant performance loss. The main reason is reduced voltage. The decrease in voltage does not appear if the temperature is reduced only in the beginning of the deposition.

- Higher substrate temperatures at 620°C again lead to a loss in performance due to reduced voltage.

- If the substrate temperature is further reduced below 450°C voltage and fill factor strongly decline, resulting in very poor performance. The current is also reduced, but very little in comparison to voltage and fill factor.

- No significant performance decay takes place if the substrate temperature is reduced in the beginning of the deposition, while held at high temperatures towards the end of the deposition.

Since fill factor and voltage are responsible for the poor performance the thickness obviously has no significant influence on the device quality.

From the results above it follows that thin high quality CIGS can be quickly deposited. High substrate temperatures are required only towards the end of the deposition.

Chapter 8

Appendix

8.1   Thermocouple data links

The following links lead to the data source of table 4.1.

    Type T `http://srdata.nist.gov/its90/download/type_t.tab`
    Type J `http://srdata.nist.gov/its90/download/type_j.tab`
    Type E `http://srdata.nist.gov/its90/download/type_e.tab`
    Type K `http://srdata.nist.gov/its90/download/type_k.tab`
    Type N `http://srdata.nist.gov/its90/download/type_n.tab`
    Type R `http://srdata.nist.gov/its90/download/type_r.tab`
    Type S `http://srdata.nist.gov/its90/download/type_s.tab`
    Type B `http://srdata.nist.gov/its90/download/type_b.tab`
    Type K `http://www.omega.com/thermocouples.html`

Bibliography

[1] M. A. Green, K. Emery, Y. Hishikawa, and W. Warta. Solar cell efficiency tables (version 36). *Progress in Photovoltaics: Research and Applications*, 18(5):346–352, 2010.

[2] C. Podewils. Der Mix wird sonnig. *Photon Das Solarstrom-Magazin*, 10:14–20, 2011.

[3] G. Henning and M. B. Krause. Mit angezogener Handbremse. *Photon Das Solarstrom-Magazin*, 10:36–40, 2011.

[4] Photovoltaic Barometer. *Systèmes Solaires le journal du photovoltaïque*, 5:144– 171, 2011.

[5] A. Goetzberger, C. Hebling, and H.-W. Schock. Photovoltaic materials, history, status and outlook. *Materials Science and Engineering: R: Reports*, 40(1):1 – 46, 2003.

[6] T. Markvart and L. Castaner. *Practical handbook of photovoltaics - fundamentals and applications*. Elsevier, New York, 2003. ISBN 1856173909.

[7] W. Shockley and H.J. Queisser. Detailed balance limit of efficiency of p-n junction solar cells. *Journal of Applied Physics*, 32(3):510–519, 1961.

[8] M. A. Green. *Third Generation Photovoltaics: Advanced Solar Energy Conversion (Volume 0)*. Springer, 8 2003. ISBN 139783540265627.

[9] S. Wagner, J. L. Shay, P. Migliorato, and H. M. Kasper. $CuInSe_2$/CdS heterojunction photovoltaic detectors. *Applied Physics Letters*, 25(8): 434–435, 1974.

[10] J. L. Shay, S. Wagner, and H. M. Kasper. Efficient $CuInSe_2$/CdS solar cells. *Applied Physics Letters*, 27(2):89–90, 1975.

[11] L. L. Kazmerski, M. S. Ayyagari, and G. A. Sanborn. CuInS$_2$ thin films: Preparation and properties. *Journal of Applied Physics*, 46(11): 4865–4869, 1975.

[12] L. L. Kazmerski, F. R. White, and G. K. Morgan. Thin - film CuInSe$_2$/CdS heterojunction solar cells. *Applied Physics Letters*, 29 (4):268–270, 1976.

[13] R. Klenk, J. Klaer, Ch. Köble, R. Mainz, S. Merdes, H. Rodriguez-Alvarez, R. Scheer, and H.W. Schock. Development of CuInS2-based solar cells and modules. *Solar Energy Materials and Solar Cells*, In Press, Corrected Proof, 2010.

[14] S. Marsillac, P. D. Paulson, M. W. Haimbodi, R. W. Birkmire, and W. N. Shafarman. High-efficiency solar cells based on Cu(InAl)Se$_2$ thin films. *Applied Physics Letters*, 81(7):1350 –1352, 2002.

[15] J. Hedstrom, H. Ohlsen, M. Bodegård, A. Kylner, L. Stolt, D. Hariskos, M. Ruckh, and H.-W. Schock. ZnO/CdS/Cu(In,Ga)Se$_2$ thin film solar cells with improved performance. In *Photovoltaic Specialists Conference, 1993., Conference Record of the Twenty Third IEEE*, pages 364 –371, May 1993.

[16] L. Stolt, J. Hedstrom, J. Kessler, M. Ruckh, K.-O. Velthaus, and H.-W. Schock. ZnO/CdS/CuInSe$_2$ thin-film solar cells with improved performance. *Applied Physics Letters*, 62(6):597–599, 1993.

[17] U. Rau and H.W. Schock. Electronic properties of Cu(In,Ga)Se$_2$ heterojunction solar cells-recent achievements, current understanding, and future challenges. *Applied Physics A: Materials Science & Processing*, 69:131–147, 1999.

[18] S. Siebentritt, M. Igalson, C. Persson, and S. Lany. The electronic structure of chalcopyrite bands, point defects and grain boundaries. *Progress in Photovoltaics: Research and Applications*, 18:390– 410, 2010.

[19] R. Klenk, T. Walter, H.-W. Schock, and D. Cahen. A model for the successful growth of polycrystalline films of CuInSe$_2$ by multisource physical vacuum evaporation. *Advanced Materials*, 5(2):114–119, 1993.

[20] K. Sakurai, R. Scheer, S. Nakamura, Y. Kimura, T. Baba, C.A. Kaufmann, A. Neisser, S. Ishizuka, A. Yamada, K. Matsubara, K. Iwata, P. Fons, H. Nakanishi, and S. Niki. Structural changes of CIGS during deposition investigated by spectroscopic light scattering: A study on Ga

concentration and Se pressure. *Solar Energy Materials and Solar Cells*, 90(18-19):3377 – 84, 2006/11/23.

[21] S. Ishizuka, H. Shibata, A. Yamada, P. Fons, K. Sakurai, K. Matsubara, and S. Niki. Growth of polycrystalline Cu(In,Ga)Se$_2$ thin films using a radio frequency-cracked Se-radical beam source and application for photovoltaic devices. *Applied Physics Letters*, 91(4):041902 – 1, 2007/07/23.

[22] S. Ishizuka, A. Yamada, H. Shibata, P. Fons, K. Sakurai, K. Matsubara, and S. Niki. Growth of Cu(In,Ga)Se$_2$ absorbers using a Se-radical beam source. In *22. European Photovoltaic Solar Energy Conference (EU PVSEC)*, pages 2308 – 2311, 2007.

[23] M.M. Islam, T. Sakurai, S. Ishizuka, A. Yamada, H. Shibata, K. Sakurai, K. Matsubara, S. Niki, and K. Akimoto. Effect of Se/(Ga+In) ratio on MBE grown Cu(In,Ga)Se$_2$ thin film solar cell. *Journal of Crystal Growth*, 311(7):2212 – 14, 2009/03/15.

[24] S. Ishizuka, A. Yamada, H. Shibata, P. Fons, K. Sakurai, K. Matsubara, and S. Niki. Large grain Cu(In,Ga)Se$_2$ thin film growth using a Se-radical beam source. *Solar Energy Materials and Solar Cells*, 93(6-7): 792 – 6, 2009/06/.

[25] M. Bodegård, L. Stolt, and J. Hedström. The influence of sodium on the grain structure of CuInSe$_2$ films for photovoltaic applications. In *12. European Photovoltaic Solar Energy Conference (EU PVSEC)*, pages 1743–1746, 1994/04/.

[26] S. Ishizuka, A. Yamada, M.M. Islam, H. Shibata, P. Fons, T. Sakurai, K. Akimoto, and S. Niki. Na-induced variations in the structural, optical, and electrical properties of Cu(In,Ga)Se$_2$ thin films. *Journal of Applied Physics*, 106(3):034908 (6 pp.) –, 2009/08/01.

[27] R. Scheer and H.-W. Schock. *Chalcogenide Photovoltaics: Physics, Technologies, and Thin Film Devices*. Wiley-VCH, 1 edition, 4 2011. ISBN 9783527314591.

[28] R. Herberholz, H.W. Schock, U. Rau, J.H. Werner, T. Haalboom, E. Giidecke, T.and Ernst, C. Beilharz, K.W. Benz, and D. Cahen. New Aspects of Phase Segregation and Junction Formation in CuInSe. In *Conference Record of the Twenty-sixth IEEE Photovoltaic Specialists Conference 1997*, pages 323 – 4, 1997//.

[29] M. Bodegård, K. Granath, and L. Stolt. Growth of Cu(In,Ga)Se$_2$ thin films by coevaporation using alkaline precursors. *Thin Solid Films*, 361-362:9 – 16, 2000/02/21.

[30] S. Ishizuka, A. Yamada, K. Matsubara, P. Fons, K. Sakurai, and S. Niki. Alkali incorporation control in Cu(In,Ga)Se$_2$ thin films using silicate thin layers and applications in enhancing flexible solar cell efficiency. *Applied Physics Letters*, 93(12):124105 (3 pp.) –, 22 Sept. 2008.

[31] S. Ishizuka, H. Hommoto, N. Kido, K. Hashimoto, A. Yamada, and S. Niki. Efficiency Enhancement of Cu(In,Ga)Se$_2$ Solar Cells Fabricated on Flexible Polyimide Substrates using Alkali-Silicate Glass Thin Layers. *Applied Physics Express*, 2008.

[32] A. Chirila, S. Buecheler, F. Pianezzi, P. Bloesch, C. Gretener, A. R. Uhl, C. Fella, L. Kranz, J. Perrenoud, S. Seyrling, R. Verma, S. Nishiwaki, Y.E. Romanyuk, G. Bilger, and A.N. Tiwari. Highly efficient Cu(In,Ga)Se$_2$ solar cells grown on flexible polymer films . *Nature Materials*, 10:857 –861, November 2011.

[33] A. M. Gabor, J. R. Tuttle, D. S. Albin, M. A. Contreras, R. Noufi, and A. M. Hermann. High-efficiency CuIn$_x$Ga$_{1-x}$Se$_2$ solar cells made from (In$_x$,Ga$_{1-x}$)$_2$Se$_3$ precursor films. *Applied Physics Letters*, 65(2):198–200, 1994.

[34] M. Nishitani, T. Negami, and T. Wada. Composition monitoring method in CuInSe$_2$ thin film preparation. *Thin Solid Films*, 258(1-2):313 – 316, 1995.

[35] N. Kohara, T. Negami, M. Nishitani, and T. Wada. Preparation of device-quality $Cu(In,Ga)Se_2$ thin films deposited by Coevaporation with composition monitor. *Japanese Journal of Applied Physics*, 34 (Part 2, No. 9A):L1141–L1144, 1995.

[36] T. Satoh, S. Hayashi, S. Nishiwaki, S. i. Shimakawa, Y. Hashimoto, T. Negami, and T. Uenoyama. Fabrication of Cu(In,Ga)Se$_2$ by in-line evaporation (composition monitoring method using heat radiation). *Solar Energy Materials and Solar Cells*, 67(1-4):203 – 207, 2001.

[37] R. Hunger, K. Sakurai, A. Yamada, P. Fons, K. Iwata, K. Matsubara, and S. Niki. In situ deposition rate monitoring during the three-stage-growth process of Cu(In,Ga)Se$_2$ absorber films. *Thin Solid Films*, 431-432:16 – 21, 2003.

[38] K. Sakurai, R. Hunger, R. Scheer, C.A. Kaufmann, A. Yamada, T. Baba, Y. Kimura, K. Matsubara, P. Fons, H. Nakanishi, and S. Niki. In situ diagnostic methods for thin-film fabrication: utilization of heat radiation and light scattering. *Progress in Photovoltaics: Research and Applications*, 12(2-3):219 – 34, 2004/03/.

[39] M. Bodegård, J. Kessler, O. Lundber, J. Schöldström, and L. Stolt. Growth of Co-Evaporated Cu(In,Ga)Se$_2$ - The Influence of Rate Profiles on Film Morphology. In *Proceedings Materials Research Society Symposium*, volume 668, 2001.

[40] T. Schlenker, H.-W. Schock, and J. H. Werner. Initial growth behavior of Cu(In,Ga)Se$_2$ on molybdenum substrates. *Journal of Crystal Growth*, 259(1-2):47 – 51, 2003.

[41] T. Schlenker, M. Luis Valero, H.-W. Schock, and J.H. Werner. Grain growth studies of thin Cu(In, Ga)Se$_2$ films. *Journal of Crystal Growth*, 264(1-3):178 – 183, 2004.

[42] M. Lammer, U. Klemm, and M. Powalla. Sodium co-evaporation for low temperature Cu(In,Ga)Se$_2$ deposition. *Thin Solid Films*, 387(1-2): 33 – 36, 2001.

[43] M. Lammer, R. Kniese, and M. Powalla. In-line deposited Cu(In,Ga)Se$_2$ solar cells: influence of deposition temperature and Na co-evaporation on carrier collection. *Thin Solid Films*, 451-452:175 – 178, 2004. Proceedings of Symposium D on Thin Film and Nano-Structured Materials for Photovoltaics, of the E-MRS 2003 Spring Conference.

[44] L. Zhang, Q. He, W.-L. Jiang, F.-F. Liu, C.-J. Li, and Y. Sun. Effects of substrate temperature on the structural and electrical properties of Cu(In,Ga)Se$_2$ thin films. *Solar Energy Materials and Solar Cells*, 93(1): 114–18, 2009.

[45] H. Wang, Y. Zhang, X. L. Kou, Y. A. Cai, W. Liu, T. Yu, J. B. Pang, C. J. Li, and Y. Sun. Effect of substrate temperature on the structural and electrical properties of CIGS films based on the one-stage co-evaporation process. *Semiconductor Science and Technology*, 25(5): 055007, 2010.

[46] U. Zimmermann, M. Ruth, and M. Edoff. Cadmium-free CIGS mini-modules with ALD-grown Zn(O, S)-based buffer layers. In *Proceedings of the 21st European Photovoltaic Solar Energy Conference*, 2006.

[47] A. Hultqvist, C. Platzer-Björkman, T. Törndahl, M. Ruth, and M. Edoff. Optimization of i-ZnO window layers for Cu(In,Ga)Se$_2$ solar cells with ALD buffers. Milan, Italy, September 2007. 22nd European Photovoltaic Solar Energy Conference.

[48] L. Platzer-Björkman, P. Zabierowski, J. Pettersson, T. Törndahl, and M. Edoff. Improved fill factor and open circuit voltage by crystalline selenium at the Cu(In,Ga)Se$_2$ / buffer layer interface in thin film solar cells. *Progress in Photovoltaics: Research and Applications*, 18(4):249–256, June 2010.

[49] J. Scholz and T. Ricolfi, editors. *Thermal Sensors, Volume 4, Sensors: A Comprehensive Survey*. Wiley-VCH, 12 1990. ISBN 9783527267705.

[50] Omega. *Temperature Handbook*. Omega Books, 2000. URL `http://www.omega.com/literature/`.

[51] S. Einarsson. An investigation and Installation of an Infrared Thermometer for substrate temperature measurements in vacuum. Master's thesis, Uppsala University, 2002.

[52] *Viewports and Glass Components*. Caburn MDC Europe Limited, www.mdcvacuum.co.uk/resources/downloads/pdfs/sec5.1.6.pdf, 2011. link visited 20120216.

[53] William N. Shafarman and Jie Zhu. Effect of substrate temperature and depostion profile on evaporated Cu(InGa)Se$_2$ films and devices. *Thin Solid Films*, 361-362:473 – 477, 2000.

[54] C. Edelmann. *Vakuumphysik: Grundlagen, Vakuumerzeugung und -messung, Anwendungen (German Edition)*. Spektrum Akademischer Verlag, 1997. ISBN 3827400074.

[55] J. F. Hanlon. *A User's Guide to Vacuum Technology*. Wiley, 1989. ISBN 9780471270522.